ORNL/TM-2024/3465

Evaluation of In-Situ AM Process Monitoring Techniques and Potential for Detecting Process Anomalies and Undesirable Microstructures

Holden C. Hyer
Brandon J. Schreiber
Daniel C. Sweeney
Christian M. Petrie

Approved for public release.
Distribution is unlimited.

July 2024

M3CR-22OR0403033

OAK RIDGE National Laboratory

ORNL IS MANAGED BY UT-BATTELLE LLC FOR THE US DEPARTMENT OF ENERGY

DOCUMENT AVAILABILITY

Reports produced after January 1, 1996, are generally available free via OSTI.GOV.

Website www.osti.gov

Reports produced before January 1, 1996, may be purchased by members of the public from the following source:

National Technical Information Service
5285 Port Royal Road
Springfield, VA 22161
Telephone 703-605-6000 (1-800-553-6847)
TDD 703-487-4639
Fax 703-605-6900
E-mail info@ntis.gov
Website http://classic.ntis.gov/

Reports are available to US Department of Energy (DOE) employees, DOE contractors, Energy Technology Data Exchange representatives, and International Nuclear Information System representatives from the following source:

Office of Scientific and Technical Information
PO Box 62
Oak Ridge, TN 37831
Telephone 865-576-8401
Fax 865-576-5728
E-mail reports@osti.gov
Website https://www.osti.gov/

ORNL/TM-2024/3465

Advanced Materials and Manufacturing Technologies

EVALUATION OF IN-SITU AM PROCESS MONITORING TECHNIQUES AND POTENTIAL FOR DETECTING PROCESS ANOMALIES AND UNDESIRABLE MICROSTRUCTURES

Holden C. Hyer
Brandon J. Schreiber
Daniel C. Sweeney
Christian M. Petrie

July 2024

Milestone #: M3CR-22OR0403033

Prepared by
OAK RIDGE NATIONAL LABORATORY
Oak Ridge, TN 37831
managed by
UT-BATTELLE LLC
for the
US DEPARTMENT OF ENERGY
under contract DE-AC05-00OR22725

CONTENTS

LIST OF FIGURES

ABBREVIATIONS

AM	additive manufacturing
AMMT	Advanced Materials and Manufacturing Technologies
APD	avalanche photodiode
ART	Advanced Reactors Technologies
ASME	American Society of Mechanical Engineers
BPVC	Boiler and Pressure Vessel Code
CAD	computer-aided design
CCD	charge-coupled device
DED	direct energy deposition
DMSCNN	Dynamic Multilabel Segmentation Convolutional Neural Network
DOE-NE	Department of Energy, Office of Nuclear Energy
DMSCNN	dynamic multilabel segmentation convolutional neural network
FBG	fiber Bragg grating
HFIR	high flux isotope reactor
HIP	hot isostatic pressing
IR	infrared
LPBF	laser powder bed fusion
MDF	Manufacturing Demonstration Facility
NIR	near infrared
OFDR	optical frequency domain reflectometry
ORNL	Oak Ridge National Laboratory
PDA	photodiode array
RTD	resistive temperature device
SNR	signal to noise ratio
SS	stainless steel
TCR	Transformational Challenge Reactor
WDM	wavelength division multiplexer
XCT	X-ray computed tomography
XRD	X-ray diffraction

ABSTRACT

The US Department of Energy's Advanced Materials and Manufacturing Technologies (AMMT) program is pursuing rapid qualification of new materials for fabrication of nuclear relevant components using advanced manufacturing techniques. Particular interest is placed on code-qualifying stainless steel (SS) 316H processed by laser powder bed fusion (LPBF) additive manufacturing. A paradigm that incorporates data from in-situ sensing during the printing, ex-situ characterization, and advanced artificial intelligence–based models was established under the Transformation Challenge Reactor (TCR) program to develop a pedigree for each fabricated component that could be tracked from the feedstock to the component's release for application. Under the TCR program, the Peregrine software was developed as a tool for incorporating the vast amounts of in-situ and ex-situ characterization data collected; all data stored on a rapidly growing digital platform. The digital platform allows for users to link site-specific process anomalies to the macro- and microstructure. The platform will eventually be able to predict component performance, which will be crucial to qualifying materials and components in risk-averse industries such as those supporting and building nuclear reactors. Current in-situ process monitoring techniques that are already integrated with software like Peregrine are advantageous for identifying process anomalies including powder spatter, component edge swelling, recoating-build interactions, and so on. However, additional data are required to fully predict the resulting microstructures needed for identifying relationships to component performance. The rapid cooling rates observed in LPBF are some of the highest of any bulk manufacturing process, resulting in heterogenous microstructures and typically causing anisotropy in mechanical properties. Moreover, evolved residual thermal stresses are high, which can cause severe defects such as delamination or cracking. Therefore, other in-situ monitoring methods are warranted for exploration to measure and map the thermal history, and potentially the stress state, of each build. This report summarizes different in-situ monitoring strategies proposed for LPBF with a focus on the more developed sensor systems. Novel capabilities for measuring melt pool temperatures are also addressed to better inform modeling efforts.

1. INTRODUCTION

In the nearly 70 years since the first commercial nuclear reactors went critical in the late 1950s, only incremental advances have been made on reactor design and the materials used to build them [1-3]. Many of the materials systems used in the 1950s included Zr alloys for fuel cladding; stainless steels (SSs) for structural components, including the pressure vessel; and some Inconel alloys used in the coolant pumps or electricity generation steam turbines [1-3]. Despite the significant advances in alloy development, advanced reactor concepts must design their components to use these same materials systems. The main challenge lies in qualification of the materials system, which relies on exhaustive testing over long durations and, in some cases, irradiation data to ensure that the materials will perform as intended.

For example, the American Society of Mechanical Engineers (ASME) Boiler and Pressure Vessel Code (BPVC) requires extensive materials testing that could take more than 20 years to satisfy all the requirements needed. Section III, Division 5 of the ASME BPVC currently only lists six alloys that have met all the requirements for qualification: SS304, SS316, Fe-2.25Cr-1Mo, Fe-9Cr-1Mo, Alloy 800H, and the most recent addition, IN617 which was added in 2020. The code case for IN617 was first drafted in the early 1990s, and the 100,000-h creep life qualification ballot was not approved as an executable until 2001 [4]. A current code case is being developed under the Advanced Reactors Technologies (ART) program of the US Department of Energy, Office of Nuclear Energy (DOE-NE) to code qualify alloy 709. Efforts into code qualifying alloy 709 for a 500,000 h creep life were first initiated in 2013, with execution starting in 2014 [5, 6]. Significant progress has been made in code qualifying 709 for a longer rupture life (500,000 h) than that approved for IN617 (100,000 h), but the time to fulfilment of the code case could still be 5–10 years [5, 6].

Qualification with conventional manufacturing typically follows a design–manufacture–test procedure, requiring extensive time to make iterations that feed back into the qualification process flow. Risk-averse industries such as nuclear are unlikely to adopt any approach that circumvents the continuous feedback and learning process [7-9]. With advanced manufacturing techniques like additive manufacturing (AM), the ability to realize complex geometries after conceptualization allows for rapid prototyping that was not possible with conventional manufacturing techniques. Geometric optimization informed by modeling and simulation can be continuously tested with the fast turnaround manufacturing provided by AM, all during the design phase, without having to wait for feedback after a component or material system is fabricated and subjected to a body of testing [9, 10]. For example, the Transformational Challenge Reactor (TCR) program sought to leverage recent advances in AM to develop and build a reactor with qualified materials such as SS316 [9, 11]. The main goal of the TCR program was to deploy advanced nuclear reactor systems that were free from the constraints of conventional manufacturing [9, 10]. The TCR program demonstrated that complex components could be designed outside the typical space provided for conventional reactor designs and could be printed and ready for evaluation and testing within one week [12, 13].

Taking a more manufacturing- and microstructure-informed approach to qualification could reduce the need for such prolonged materials code case efforts. DOE-NE launched the Advanced Materials and Manufacturing Technologies (AMMT) program to establish a rapid qualification framework that includes evaluation of desired materials using advanced manufacturing techniques and their performance in nuclear reactor environments to eventually be used for components deployed in nuclear reactors [14, 15]. The AMMT program has identified that laser powder bed fusion (LPBF), wire-arc direct energy deposition (DED), and large-scale hot isostatic pressing (HIP) are the most diverse, most applicable advanced manufacturing techniques currently available. Particular focus has been placed on LPBF because of its unique advantage for realizing fine features (>100 μm) and the extensive work already performed and published in the literature.

LPBF involves the selective melting of a powder bed by a laser source, additively building material layer by layer [16]. The LPBF cooling rates are some of the fastest of any bulk manufacturing process, on the order of 10^6–10^7 K/s, inherent to continuous localized melting [17-19]. Consequently, the complex melting and subsequent solidification can result in multiple process anomalies, as well as evolution of high residual strains that could lead to component failure. Uncertainties persist in the identification of process anomalies and the assessment of their effect on the component's integrity, microstructure, and properties. A foundation for monitoring and identifying process anomalies in situ during the LPBF process was developed under the TCR program [20, 21]. The general approach relies on recent advances in artificial intelligence, modeling and simulation, in-situ sensing, and ex-situ characterization to build a fully integrated profile of a component from cradle to grave [20, 21]. Using a digital platform, in-situ sensing data can be correlated and superimposed with site specific ex-situ characterization data that may include microscopy or mechanical test data. Ideally, maintenance of a digital twin of the component will inform iterative designs and AM processing as a feedback method towards rapid qualification without the need to always rely on exhaustive testing to build needed confidence.

Reducing uncertainty in each build processed by LPBF requires proper in-situ sensing as a first stop measure along the life of qualifying a material system or component. Numerous techniques have been identified for in-situ monitoring in LPBF [22], as detailed in the schematic shown in Figure 1. However, most of these techniques are expensive and/or are immature and still require extensive testing before they can be properly used in commercial applications. Probe-based sensors are already used to measure environmental factors such as the temperature or O_2 content of the build chamber. Probe sensors may also be embedded within the build plate or build volume to measure subsurface temperatures, residual strain, and other metrics. Waveform techniques such as eddy current or acoustic sensing are used frequently to find defects or cracks in welds and other components, but they have not been investigated to the extent necessary to triangulate defects to specific locations, which would be required in LPBF. Synchrotron and neutron-based source methods are powerful tools; however, it is expensive to build and maintain sources, which only really exist at national laboratories or universities for research purposes. X-ray sources are becoming more common for imaging and inspection, but they are not optimized for sustained in-situ monitoring of multiple builds [23]. X-rays are more useful in ex-situ techniques such as X-ray computed tomography (XCT) or X-ray diffraction (XRD) [24].

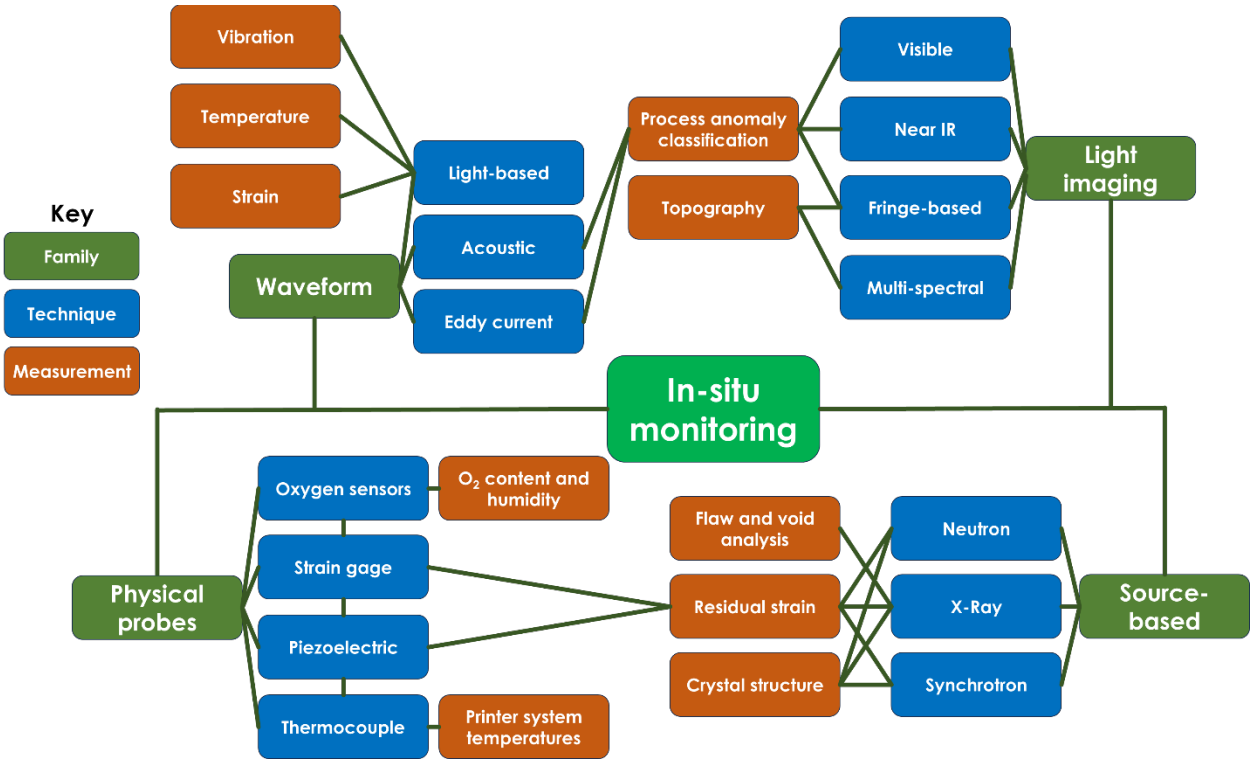

Figure 1. Summary of various sensing techniques and their application for in-situ monitoring in LPBF.

The most prevalent method for monitoring a build is to image the powder bed before and after each successive layer. Machine vision algorithms translate the collected images into a common coordinate system and machine-learning algorithms are used to sift through and classify individual voxels [25-29]. Different process anomalies such as porosity, swelling, poor powder spreading, and others can be identified as classes, and the machine learning algorithm can be trained to detect these anomalies. Depending on the quality and number of diverse builds analyzed, the algorithms may be capable of identifying process anomalies, but there is still no justifiable confidence level available to quantify the acceptability of said anomalies and their potential effects on part quality.

LPBF process anomalies could potentially induce flaws, voids, or other defects in the macro- and microstructure. The inherently high cooling rates in LPBF are host to fast solidification kinetics, often resulting in heterogenous microstructures full of anisotropic grain morphology with high aspect ratios. High cooling rates may also result in solute segregation to a subgrain dendritic/cellular structure [30]. The laser interaction with the powder bed is proportional to the geometry of the melt pool formed, which is proportional to the resulting macro- and microstructure [31, 32]. For example, high laser energy input can lead to boiling of the molten metal, causing deep penetration (i.e., keyholing), often leaving behind pores from unescaped gases. Transitioning to low laser energy inputs may result in insufficient melting between powder particles, often leaving behind irregular pores caused by lack of fusion [33].

Better quantification of the melt pool behavior could be used to help correlate the detected process anomalies to the resulting macro- and microstructure. Faster cooling rates (lower laser energy input) typically result in finer grain structures, but the evolved residual stresses might be high compared to those that would otherwise result if a slower cooling rate were induced (higher laser energy input). The objective is to find the balance between reducing the aspect ratio in the grain morphology and the amount of stress a material can accommodate before failure is observed. Currently, photodiodes and or near infrared (NIR) imaging can be used to provide some temperature information, often measuring intensity

differences across the build [34, 35]. However, it is difficult to calibrate the intensities recorded from some of these devices to a true temperature and also be able to capture the rapid cooling kinetics. Instruments such as high-speed charge-coupled device (CCD) cameras and pyrometers are designed to measure the temperature profile of focused point sources. Capturing the true temperature of the melt pool, or at least capturing the cooling curve, would require balancing fast sampling rates in a manner similar to that used to measure the cooling rates of LPBF while maintaining accuracy and field of view.

Accumulated residual strain is directly related to the changes in the material's thermal expansion with temperature. The laser melting instantaneously increases the temperature of the system and almost instantly reverts back to a solid, locking in the localized deformation. The stress state of the system near the end of solidification could cause shearing at the grain boundaries of newly formed grains, thus creating a cavity [36]. If the material cannot accommodate the evolving stresses, then the newly formed cavities could propagate along a grain boundary, leading to cracking [36, 37]. If cracking is not observed because of crack healing (e.g., liquid backflow into cavities), then the accumulated stress may still overcome the yielding point of the material, causing the component to begin to plastically deform. Stress-induced deformation includes warpage or total delamination between layers.

Probe sensors such as piezoelectrics or fiber optics can be embedded within the build plate or build volume to measure the changes in stress, but they are not ideal for continuous mapping of the entire build volume [38]. Ideally, source-based in-situ methods (Figure 1) such as XRD can be used to measure the accumulated stress during a build, but penetration and resolution issues currently limit the technology [23]. Therefore, source-based methods are best for providing post-build characterization to validate the evolved strains within component(s). A different approach would be to monitor excessive changes in stress that would cause part failure to stop a build or notify the operator before a machine learning set-up would determine the severity of a particular anomaly. As has been performed across multiple industries for years, including nuclear, acoustic waveforms can be used to detect defects such as cracking. Similar methodologies can be applied to LPBF. Commercial LPBF systems will be host to many vibrations from the gas-recirculation pump, inert gas inlet, and other components [39]. These vibrations can be monitored using acoustic sensors such as accelerometers. It has been shown that cracking and other internal defects that are severe enough to fail a printing component can be registered based on changes in the harmonic profile of the system [39, 40]. Triangulating the location of defects using acoustic sensing is difficult, but these types of sensors could be installed in a commercial system in conjunction with a kill switch to respond to more significant defects [22, 41]. Many of these defects may not be obvious or even observable to the machine learning algorithms using imaging data of the build surface.

Real-time monitoring of components during LPBF processing is vital for reducing the uncertainty in performance post-building. The uncertainty stems from the repetitive localized melting of the laser source, resulting in a complex thermal history unlike that found in conventional manufacturing processes. Varying the laser energy input will significantly affect the resulting macro- and microstructure during solidification. Sophisticated machine learning algorithms can be used to sieve and classify process anomalies detected in visible and NIR images taken during the build. Better quantification of the thermal history of the LPBF process can be correlated with the observed process anomalies, improving the ability to make informed decisions on the true quality of the printed component. Qualification of new materials and components for the nuclear industry is rigorous and would be greatly enhanced by improving quality assurance methods used during the manufacturing process.

2. RAPID SOLIDIFICATION KINETICS IN LPBF

2.1 ENERGY DENSITY

Solidification kinetics in LPBF are highly dependent on the processing parameters used to build material. The total laser energy input can be effectively related to the energy density (ED) of the system given by the following equation:

$$ED = \frac{P}{V \times HS \times LT}, \quad (1)$$

where P is the laser power, V is raster velocity, HS is the distance between consecutive laser scans (i.e., hatch spacing), and LT is the powder layer thickness [19]. For pulsed laser systems such as those used in this report, the velocity is defined by:

$$V = \frac{PD}{DT + OT}, \quad (2)$$

where PD is the distance between consecutive points that the laser hops (i.e., point distance), DT is the dwell time at each point, and OT is the dead time during which the laser is off [19]. The energy density parameters are considered the most influential on the resulting macro- and microstructure of a component.

Although some material bases (e.g., Fe-based alloy systems) have similar behaviors, the energy density parameters must be mapped to provide an understanding of a given alloy's behavior under LPBF. Generally, three regimes exist for a printable composition, as shown in Figure 2(a): (1) irregular pores from lack of fusion between the particles resulting from insufficient energy to melt, (2) a dense structure with minimum porosity, and (3) circular porosity from keyholing, which is typically caused by a high energy density [19]. Ideally, the optimized condition is one in which dense material is printed. The window for processability is potentially large for some alloys like SS316, making it difficult to choose the optimized parameter based solely on porosity content.

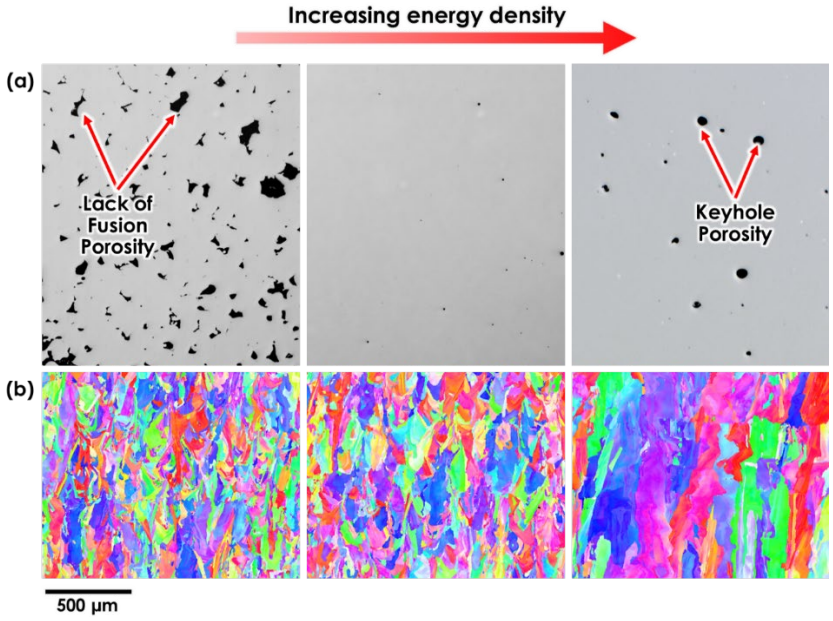

Figure 2. (a) Optical images and (b) EBSD grain maps of SS316L processed with different energy densities.

Higher energy densities typically correspond to higher heat inputs, which results in a longer time to cool to an equilibrium temperature, or lower cooling rate. More time to cool promotes grain growth, generally because the larger grains have slower cooling rates (i.e., higher energy densities) [42], as shown in Figure 2(b). Therefore, choosing the lowest energy density possible, chooses the lowest cooling rate, with the hope achieving the most refined grain structure possible. Observed grain structures in LPBF-processed material like SS316 typically consist of columnar grains with high aspect ratios oriented along the build direction. The layer-by-layer process is conducive to epitaxial growth through multiple layers of material, inevitably building the grains up in a columnar fashion. Even in materials without observable cracking, the high aspect ratio of grains in one direction causes anisotropy that has often been observed to affect performance metrics such as the tensile strength when loading the material parallel instead of perpendicular to the build direction. It is possible that columnar structures could be eliminated by using lower energy densities and changing the laser scan trajectory. However, stochastic flaw formation is still possible because local conditions in the melt pool or environmental conditions in the build chamber could vary.

2.2 Measurable Fundamental Factors

It is well established that LPBF processing of SS316 results in a microstructure containing a subgrain cellular structure in which the intercellular boundaries are enriched in solute elements such as Cr, Ni, Mo, and others [19]. Constitutional supercooling governs the formation of cellular structures, with cooling rate—a product of the thermal gradient and solid growth velocity—dictating the cell size [19]. As shown in Figure 3(a), high energy densities typically result in larger melt pools and larger cell sizes, whereas use of lower energy densities produces smaller melt pools containing smaller cell sizes. The relationship between the cooling rate ($\dot{T}$) during solidification and cell size (λ) is defined as:

$$\lambda = A\dot{T}^{-n}, \tag{3}$$

where A and n are empirically determined constants [43]. As is shown in Figure 3(b), for SS316 samples processed with different layer thicknesses and laser dwell times, the measured cell size can be used to calculate the cooling rate as a function of energy density.

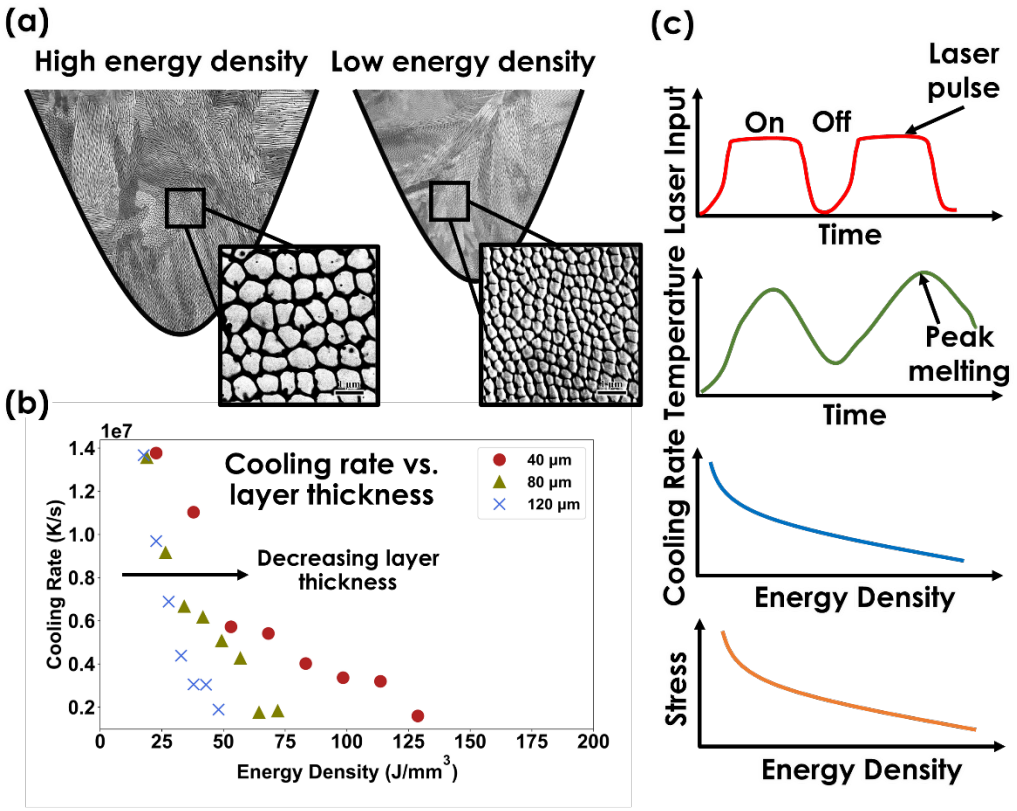

Figure 3. (a) Backscatter electron micrographs comparing melt pools and subgrain cellular structures of SS316 using a high and low energy density [19]; (b) calculated cooling rate as a function of energy density for samples printed with varying layer thicknesses [19], and (c) expected thermal history behavior based on laser input and energy density.

Estimating the cooling rates during ex-situ characterization has evidenced the strong dependence of the resulting microstructure on the thermal input into the system [19]. Pulsing the laser requires turning the laser off and on repeatedly, with a hardwired 10 µs dead time when the laser is off, regardless of the user-defined dwell time when the laser is turned on, as shown in Figure 3(c). A quasi-thermal cycling is expected each time the laser is turned off and on, heating during the defined dwell time, and cooling on the order of 10–200 K during the dead time. At some point in the localized laser melting, a peak temperature will have been reached for a given area, as shown in Figure 3(c), and a subsequent cooling curve can be extracted. Cooling rates could be measured in situ for varying energy densities to generate a calibration curve, as shown in Figure 3(c). Associated macro- and microstructure could be added to the calibration curve later to correlate any process anomalies and the grain/melt pool/cell growth to the cooling rate.

Building complex geometries with overhangs and thin-walled features will lead to variations in cooling rate, even if the same processing parameters (i.e., same energy density) are used. Because cooling rates are a fundamental parameter, they can be used as a measure to quickly identify variations in thermal history within a complex component. Changes in the cooling rate can inform the user of the effects of site-specific differences in geometries, and they also can be used to identify the microstructure associated with the measured cooling rate. Ideally, fundamental cooling rate data could be used as an input for modeling and simulation tools rather than having to model point sources and the LPBF processing parameters themselves. Moreover, the relationship between temperature and thermal strain could also be used to understand the stress state of the system [44], as shown in Figure 3(c). Predicting the stress state

would provide additional information for detecting the onset of failure in a specific region of a component that results from highly evolved residual stresses.

3. PROCESS ANOMALY DETECTION

3.1 DUAL IMAGING

The Manufacturing Demonstration Facility (MDF) at Oak Ridge National Laboratory (ORNL) has patented and licensed a deep learning algorithm called the Dynamic Multilabel Segmentation Convolutional Neural Network (DMSCNN) within the ORNL-developed Peregrine software. This software provides for in-situ process monitoring, storage of ex-situ characterization data, correlation between in-situ and ex-situ data, and connection to the digital platform [21, 27-29, 45-48]. Each component printed with LPBF starts as a computer-aided design (CAD), providing a 3D representation in a preferred coordinate system. Desired CAD files are set up in a software to organize the desired location of each component on a build plate. The file is then sliced with the given layer thickness, and 2D images are generated with the laser scan paths. Standard process anomaly sensor suites include visible light and/or near infrared cameras. Images are repetitively acquired before and after each successive layer during LPBF processing. Peregrine can then register the spatial location of collected in-situ data, laser scan paths, and any post-build characterization to the CAD files.

A Renishaw AM400 LPBF system, shown in Figure 4(a), was instrumented this fiscal year with visible and NIR cameras, as shown in Figure 4(b). The AM400 was originally thought to house the cameras in enclosures to prevent exposure to powder, as shown in Figure 4(c), because the design of the AM400 required mounting the cameras inside the build chamber. However, because the cameras were in the build chamber, they over heated and could not continuously collect data throughout a build. Once the enclosures were removed, additional iterations on the mounting design included adding a cooling channel, heat-sync fins, and aluminum mounting fixtures—all measures taken to help with heat dissipation. Additionally, software changes were made to account for any noise induced from the effects of temperature. The cameras can now sustain reasonable operating temperatures throughout the longest builds (7 days).

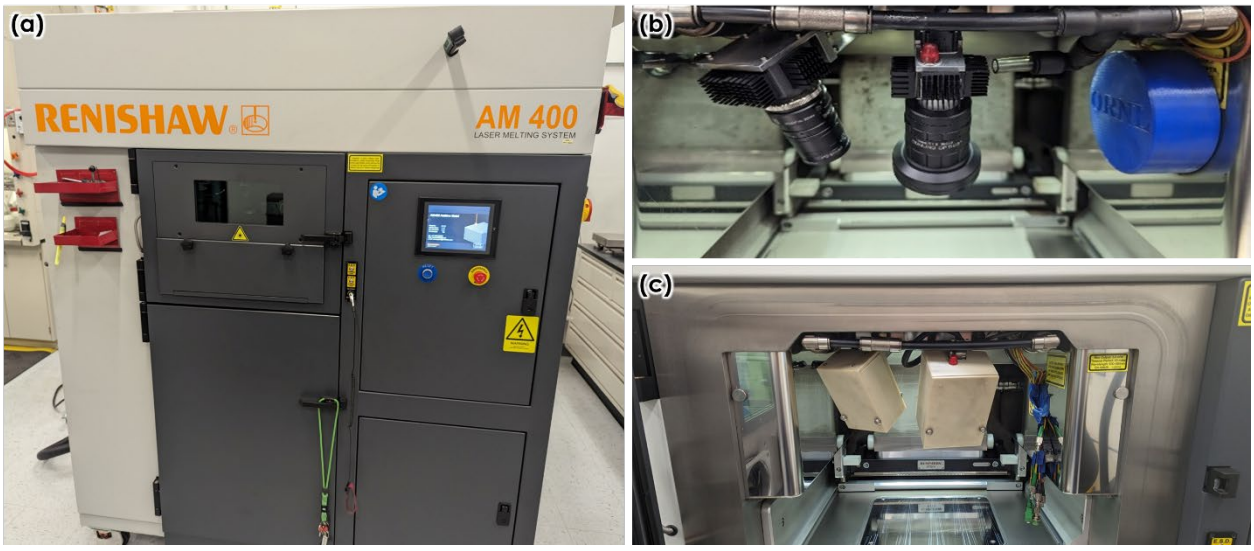

Figure 4. (a) The Renishaw AM400 LPBF system and (b, c) the visible/NIR cameras used for in-situ monitoring on the inside of the build chamber (b) in the current setup, and (c) in the original setup using enclosures for the cameras.

Peregrine is currently employed for every build on the AM400, regardless of material used. Data processing includes using the DMSCNN integrated into Peregrine. The DMSCNN divides each image into individual voxels (typically measuring 100 × 100 µm, depending on the resolution of the system), with the thickness dimension of the voxel element being equal to the layer thickness (typically 50 µm for SS316). Currently, the DMSCNN can classify the voxels based on 18 different process-related features, ranging from identifiable printed regions to regions in which process anomalies were observed. Each printer is outfitted with sensors and has its own neural network using the DMSCNN. The neural network on the AM400 is still immature and requires supervised annotation, but each printed build provides more data to help train the algorithm in the right direction.

An example of a build printed on the AM400, which is monitored using Peregrine, and processed using the DMSCNN is shown in Figure 4(a). This build is described in more detail in in Section 5 when discussing ex-situ neutron diffraction measurements. In short, two distinct plates were printed: one standing along the build direction, and the other laid flat. The plates are divided into eight discrete segments, each of which is printed with a different energy density; the energy was increased moving from left to right. Real-time monitoring can allow for the overlaying of all process anomaly classifications detected in the build, as shown in Figure 4(b) or separated individually.

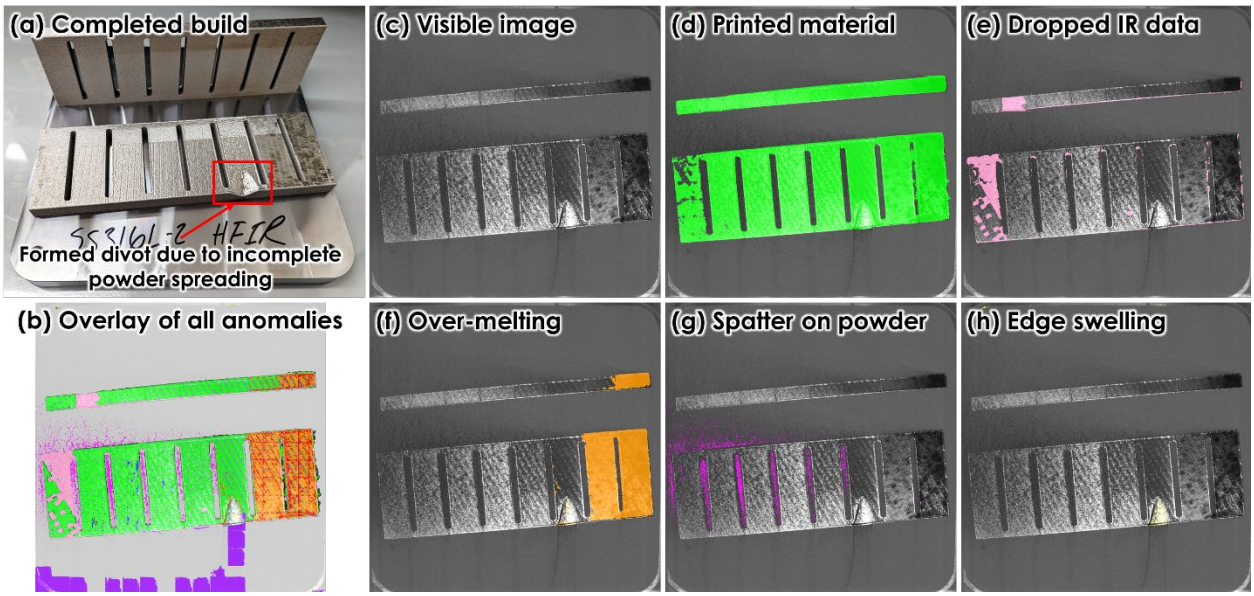

Figure 5. Process anomaly detection example of a build printed on the AM400. (a) Build included two identical plates, one stood up in the build direction, and the other laid flat on the build plate; (b) real-time monitoring detection of process anomalies can overlay everything that has been detected on a single layer from (c) a visible image; some classifications identified by the DMSCNN include (d) printed material, (e) regions in which an IR image was dropped, (f) over-melting from excessive heat input, (g) powder particle spatter, and (h) edge swelling.

For a single layer, as shown in Figure 4(c), the majority of the plate found can be considered printed material, as shown in Figure 4(d). However, a few dropped IR data were observed, as seen in Figure 4(e). The dropped data appear to correlate with areas in which there was no printed material detected on the component. More useful information from the neural network classification can also be extracted, such as the spatter on the powder bed shown in Figure 4(g). Argon is flowed as an inert shroud from right to left with respect to the images in Figure 4. The laser interaction with the powder volume is chaotic and produces spatter, which is often referred to as *soot*. These spatter particles have been linked to defect formation such as lack of fusion porosity [29]. As shown in Figure 4(g), the spatter density is higher on

the left than on the right because the Ar flow carries the spatter over so that it is often redeposited on the powder bed.

Additionally, the neural network detected the edge swelling shown in Figure 4(h), which was caused by a formed divot as indicated in Figure 4(a). Besides process-inherent, process-induced anomalies like powder spatter, the neural network identified a major flaw. The divot formed because of insufficient powder dosing, thus causing starvation on the one particular region of the component. The farthest location where printed material is found from the dosing position (back of the images in Figure 4), is the lower corner of the flat plate on the left. However, the divot formed farther right on one of the segments. In this case, the fifth segment from the left formed a divot because of starvation, because a higher energy density was used in that segment than those on the left, causing more spatter and leaving less powder behind to melt and fuse to the base.

3.2 FRINGE SYSTEM

The data shown in Figure 4 are a testament to the abilities of Peregrine and DMSCNN to properly detect process anomalies in situ during LPBF processing. Currently, the DMSCNN integrated into Peregrine classifies voxels into different categories of printing features or process anomalies. In a similar vein, the company Phase3D has pioneered the ability to perform fringe imaging in situ with LPBF to develop a topographic map of the build and to detect process anomalies from the topography. Fringe imaging relies on the projection of a repeated pattern that is typically in the form of vertical fringes on the surface in question. Images are taken of the overlayed fringe pattern for comparison to images of the expected fringe pattern to find distortions in the overlaid pattern. The distortions can be used to reconstruct a 3D profile of the surface and potentially of an entire object.

Phase3D developed a commercially available fringe system to retrofit commercial LPBF systems and is being adopted in industry. Therefore, Phase3D was selected to instrument a Renishaw AM250, pictured in Figure 6(a), which is nearly identical to the AM400, Phase3D's Fringe System. The objective is to evaluate the Fringe System's capability to better inform industry regarding its application and to complement the current method for process anomaly detection using Peregrine and the DMSCNN. Since the Fringe system produces a topographic profile, it can potentially identify the presence of pores or the propagation of defects like cracking. Although data collected by the Fringe System will be processed with Phase3D's proprietary software, it will eventually be processed in Peregrine for integration into the digital platform.

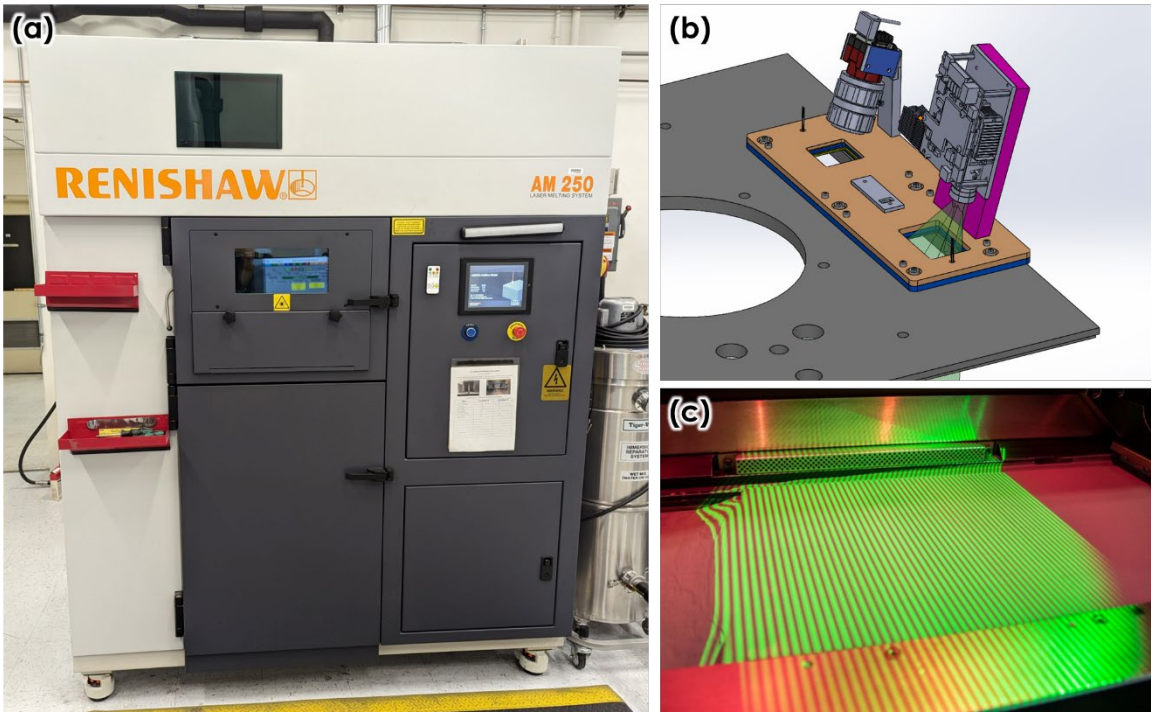

Figure 6. (a) The Renishaw AM250; (b) the proposed plan for mounting the Phase3D Fringe system on top of the AM250 build chamber; and (c) an example of the fringe projection over the build volume in an LPBF system.

A purchase order has been released, and the engineering phase has begun to design and fabricate the necessary components for outfitting the AM250's build chamber with the Fringe System, which includes a fringe projection system, a visible light camera, and various photodetectors and motion detection systems for image triggering. Initial mock-ups of the camera and projection system are shown in Figure 6(b). Cameras are to be mounted on top of the build chamber, above a feedthrough for an old light fixture. An example of the overlaid fringe projection on the powder volume is shown in Figure 6(c).

4. HIGH-SPEED PYROMETER TEMPERATURE MEASUREMENTS

4.1 MOTIVATION

Temperature probe sensors such as thermocouples or resistive temperature devices (RTDs) rely on physical heating of the probe and are not ideal for measuring rapid temperature changes. One option for measuring temperatures at high speed is to collect the radiating spectrum from the surface. For example, NIR cameras can be used to measure 2D surface temperature maps [48]. There are challenges with calibration of the NIR signal to a temperature because of variations in material emissivity that occur during laser melting [48, 49]. The spatial resolution of these techniques is also limited by the pixel size as shown in Figure 7. Depending on the resolution of the cameras used, only a few pixels may spread over the melt pool made by the weld bead, lowering accuracy of any collected data in such a small region. There is generally a tradeoff between pixel size or number of pixels and the processing time (affects maximum data acquisition rate). This last point is the primary concern with measuring cooling rates during LPBF processing. NIR cameras would never be able to collect data fast enough to accurately measure cooling rates on the order of 10^6–10^7 K/s or be able to avoid the plasma plume that is generated during laser interaction. The plume would obscure any spectrum from the laser melting, adding another layer of complication to calibration.

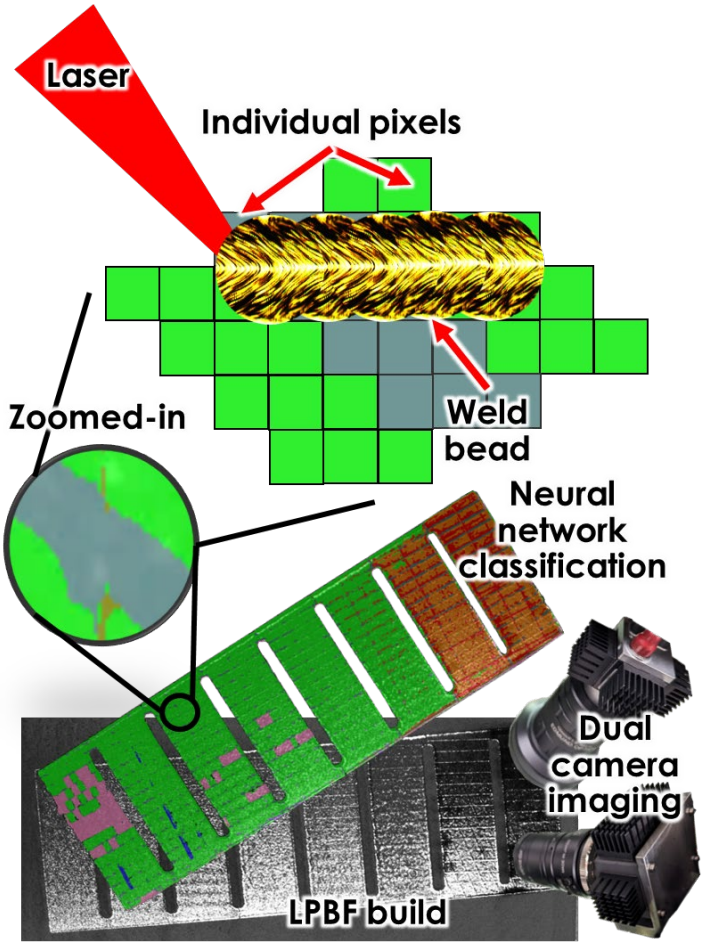

Figure 7. Demonstrating the localization of melt pools vs. the pixel resolution of Peregrine.

Pyrometry is similar to NIR cameras because it involves collection of radiating light, but the transmitted light is directed to one or more photodetectors rather than being collected as a mapped image [49]. Commercially available pyrometers are often multiwavelength because of their simple design and ease in signal processing, thus allowing for faster collection than that of NIR cameras. In particular, two-color pyrometers are attractive because they can be used independent of the emissivity once initial calibration is performed [49]. Free space optics can be used to collect light over large or small fields of view. Collected spectra can be almost instantaneously transferred to photodetectors using small fiber optics (<1 mm diameter). Pyrometer sampling can be quite fast and is purely related to the collection method and the electronics used to sample data, without having to be concerned with pixel size or resolution. Therefore, two-color pyrometers can be used to collect at high speeds that are the same speed or faster than that of the cooling rates inherent to LPBF.

4.2 CONFIGURATION AND ITERATIONS

Building the high-speed pyrometer presented a significant challenge. The design underwent many iterations based on the experiences observed. A timeline of the original iterations is given in Figure 8. Pyrometry relies on the collection of a radiation light spectrum to calibrate to a temperature. The spectral radiance (β) of a material heated to a temperature (T) at a given wavelength (λ) can be approximated using Planck's Law [50]:

$$\beta_\lambda(T) = \frac{C_1}{\lambda^5}\left[exp\left(\frac{C_2}{\lambda T}\right) - 1\right]^{-1}, \tag{4}$$

The expected intensity (I) from each wavelength can be calculated using Wein's approximation [49, 50]:

$$I_\lambda = \frac{C_1 \varepsilon_\lambda}{\lambda^5 e^{\frac{C_2}{\lambda T}}}, \tag{5}$$

where C_1 and C_2 are Planck's radiation constants, and ε_λ is the wavelength-dependent emissivity of the material. The temperature-dependent ratio (R) between intensities (I_1, I_2) for a two-color pyrometer is expressed as:

$$R(T) = \frac{I_1(T)}{I_2(T)}, \tag{6}$$

The relationship between the ratio temperature (T_R) and the actual temperature (T) can be correlated together through:

$$T_R = \left(\frac{1}{T} + \frac{\log\left(\frac{\varepsilon_1}{\varepsilon_2}\right)}{C_2(\lambda_2^{-1} - \lambda_1^{-1})}\right)^{-1}, \tag{7}$$

Eq. (7) can be rearranged to solve directly for the temperature:

$$T = \left(\frac{1}{C_2(\lambda_2^{-1}-\lambda_1^{-1}) \times log\left(\frac{R}{R_0}\right) + \log\left(\frac{\varepsilon_2 C_{1,1} \lambda_1^5}{\varepsilon_1 C_{1,2} \lambda_2^5}\right)} + \frac{\log\left(\frac{\varepsilon_1}{\varepsilon_2}\right)}{C_2(\lambda_2^{-1}-\lambda_1^{-1})}\right)^{-1}, \tag{8}$$

Using Planck's law and Wein's approximation in Eqs. (4)–(8), spectral curves can be calculated as shown in Figure 8 based on black-body radiation; the peak intensity is typically in the NIR region of wavelengths, but with increasing temperature, the peak intensity shifts to lower wavelengths.

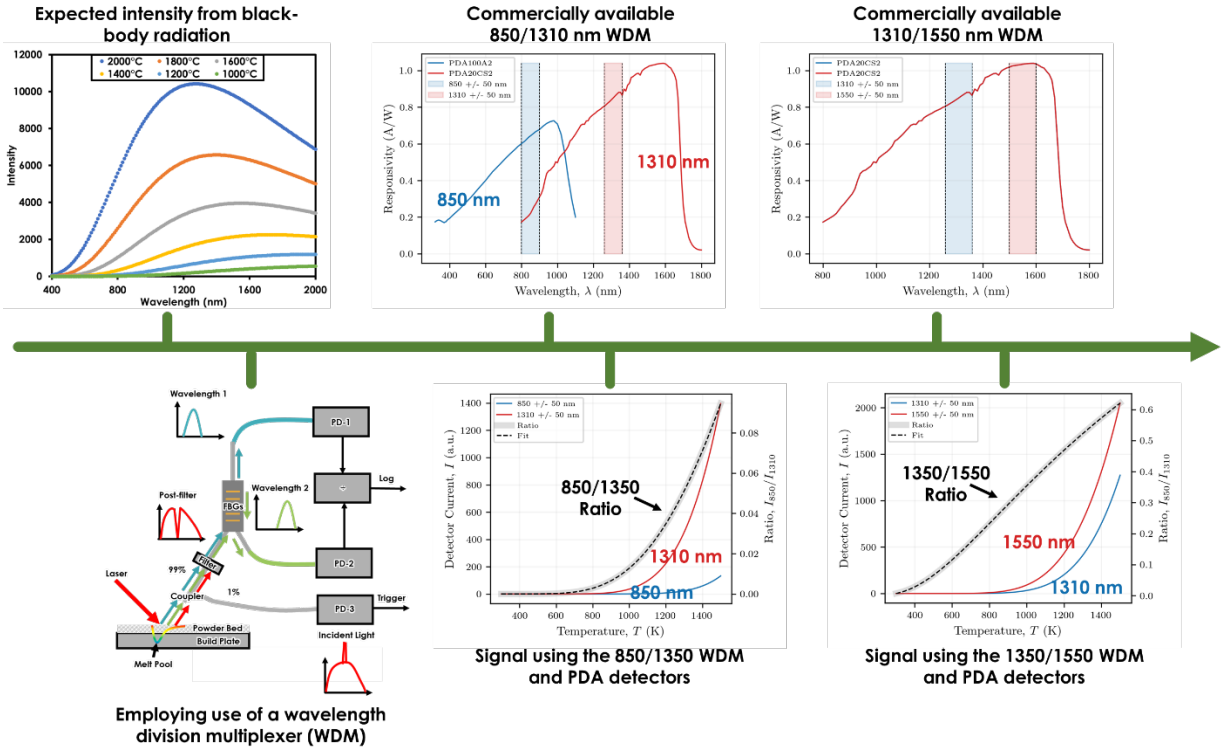

Figure 8. Thought process for fabricating the two-color pyrometer using a wavelength division multiplexer (WDM). Starting from black-body radiation curves, it was decided to use a WDM to extract two discrete wavelengths so the ratio of intensities could be calibrated to a temperature. Commercial WDMs were purchased, starting with an 850/1,350 nm WDM, but because the signal-to-noise ratio (SNR) was low, focus shifted to two higher wavelengths (1,350/1,550 nm) because the SNR increased.

It was initially thought that a two-color pyrometer would operate best by extracting two distinct wavelengths from relatively low and high wavelengths to use to take the ratio, as shown in Eq. (6). Commercially available wavelength division multiplexers (WDMs) can be procured to collect a broadband spectrum and split light using fiber Bragg gratings (FBGs) on a multimode fiber optic. FBGs are periodic modulations of the refractive index within the glass fiber that reflect specific wavelengths. In this case, the WDM would transmit one wavelength and reflect the remainder, as shown in Figure 8. The first iteration of the pyrometer used an 850/1,310 nm WDM that was directed to two adjustable gain photodetectors to collect the transmitted signal. A silicon (Si) photodetector that was sensitive in the range of 320–1,100 nm was used to collect the 850 nm output from the WDM, whereas an indium gallium arsenide (InGaAs) that was sensitive to the range of 900–1,700 nm was used to collect the 1,310 nm signal. Signal was indeed collected at both photodetectors, but the gain was maximized at 70 dB, and much of the signal was found to originate from the laser. The signal-to-noise ratio (SNR) was found to be quite high when using the 850/1,310 nm WDM. It was expected that the WDM would remove the signal intensity from the laser, but the WDM was not effective enough at filtering such an intense light source.

As seen in the timeline presented in Figure 8, an attempt was made to shift the wavelength to the higher end using a 1,310/1,550 nm WDM and swapping the Si photodetector out for a second InGaAs detector, expecting that the InGaAs detector would improve the signal by 30% as shown in Figure 8. Overall, the SNR with the new WDM was higher with limited observation of the laser, but the calculated signal ratio at 1,310 nm vs. at 1,550 nm was only slightly higher. Moreover, there were multiple issues with resolving usable data from this setup, namely *divide by zero* errors when calculating the ratio of the signals because their sensed value frequently dropped below 0. Another issue was found with determining how much if any of the signal obtained was truly melt pool radiation and not radiation from the laser. It was clear that

extracting only two distinct wavelengths would not provide the signal needed. Additional iterations included increasing the fiber diameter from 62.5 µm to 400 µm, utilizing silver-coated collimators to improve the field of view in collection, redesigning the in-situ method of radiation collection to drastically improve signal strength, and changing the photodetectors to improve gain settings and bandwidth.

Revisiting the black-body radiation curves, accounting for the detection limits of the photodetectors, it was determined that the best path forward was to collect a range of wavelengths instead of collecting discrete wavelengths. As shown in the next timeline in Figure 9, a dichroic mirror was chosen to split the broadband spectrum into two ranges of wavelengths: low (900–1,450 nm) and high (1,550–2,000 nm). It was demonstrated that the photodiode array (PDA) (non-avalanched) InGaAs detectors acquired during the WDM experimentation could be used to collect the reflected (low) and transmitted (high) wavelength ranges properly. In addition, a notch filter was added to the low wavelength side to cut out the signal at wavelengths near 1,070 nm, which is the wavelength of the laser. However, during in-situ testing, the laser signal was still observed in the photodetector data. The pyrometer setup was connected to a W halogen source to determine the efficacy of the notch filter. As can be seen in Figure 9, the notch filter cuts out >95% of the signal near 1,070 nm, but it certainly does not eliminate all the signal. Moreover, it was found that the responsivity of the PDA detectors was low when using faster collection rates. Therefore, new avalanche photodiode (APD) InGaAs detectors were acquired that do not appear to reduce responsivity at high wavelengths when compared to low wavelengths at the end of the timeline shown in Figure 9.

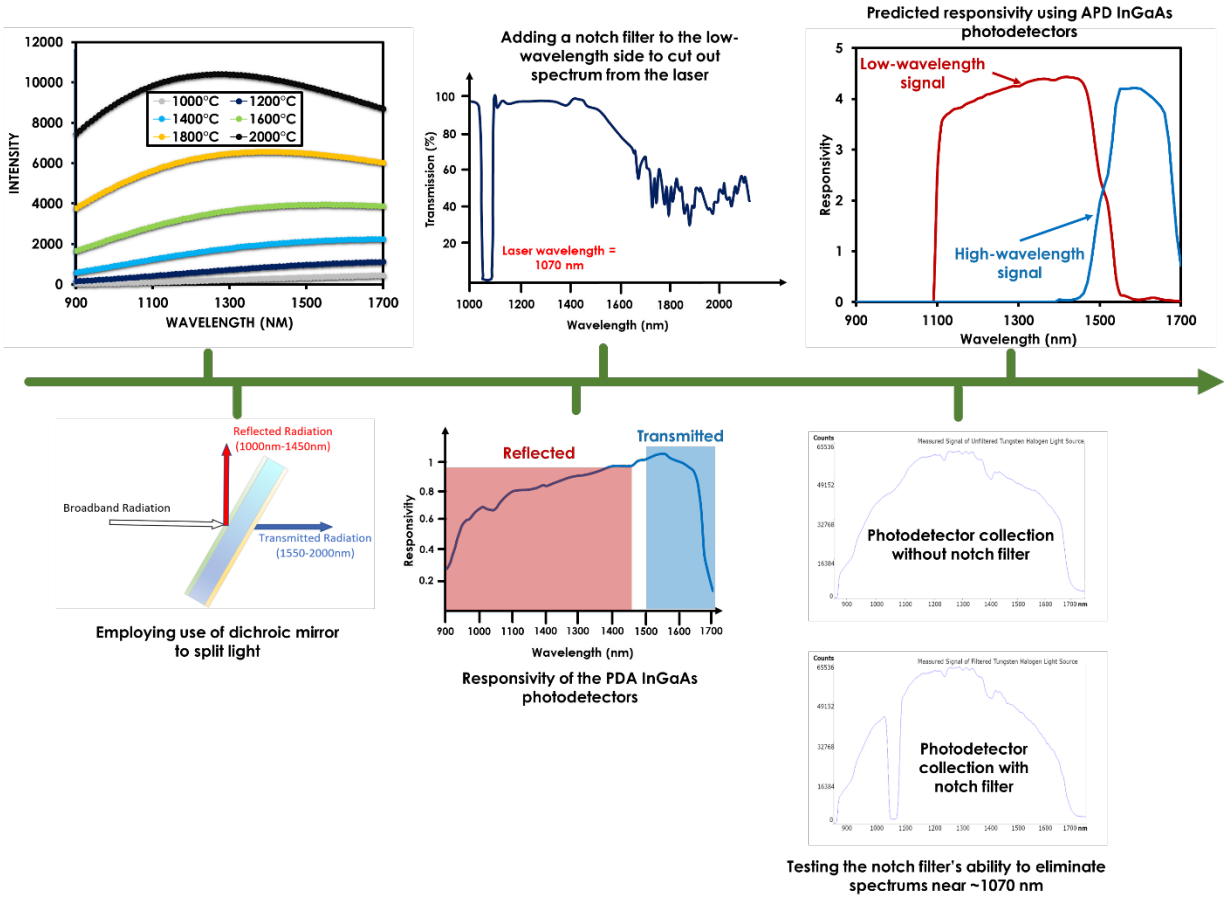

Figure 9. Thought process revisiting the black-body radiation curves with the choice to divide the collected broadband spectrum from the melt pool into two wavelength ranges using a dichroic mirror rather than basing the pyrometer on a ratio between two discrete wavelengths separated with a WDM. InGaAs detectors were originally chosen to collect the reflected and transmitted spectra from the dichroic mirror. Notch filters were added to the low wavelength end of collection to cut out the wavelength of the laser. However, it was later observed that the notch filter does not completely cut out the laser's signal, and an edgepass filter was fitted to the setup to completely remove wavelengths below 1100 nm. APD detectors were required to increase the gain after having to cut out so much of the spectrum to remove any signal from the laser.

The current setup of the pyrometer is shown in Figure 10. Based on feedback from past designs of the two-color pyrometer, the system now includes a plano-convex lens to collect the melt pool broadband spectrum and focus it to a fine point. A 400 µm diameter fiber optic is used to transmit the focused spectrum to a fixed focus collimation package. The collimated light is directed at a 1,500 nm dichroic mirror to split the signal to a low and high side. A notch filter was fitted on the lens stack to the low wavelength side before collection at the photodetector to eliminate the signal of the laser. As mentioned above, the notch filter was not fully cutting out the laser's signal. One important note is that the high-side photodetector did not pick up any stray signal from the laser. This points to the fact that either the dichroic mirror or the 1,400 nm edgepass filter are sufficiently preventing the 1,070 nm signal from the Renishaw laser from reaching the high-side photodetector. An edgepass filter now sits where the notch filer did, completely filtering out light below 1,100 nm, to ensure that the laser signal is no longer observed. On the high side, an edgepass filter is used to cut wavelengths <1,400 nm. Both photodetectors utilize InGaAs photodiodes sensitive in the range 900–1,700 nm. The previously utilized non-avalanche PDAs had an advertised bandwidth of 13 MHz, which would have been sufficient to capture the cooling rate of the melt pool. However, the bandwidth drastically decreased as the gain was increased, resulting in only a 3 kHz bandwidth at max gain. In contrast, the avalanche photodetectors retained a 10 MHz

bandwidth at their maximum gain settings, which was more than appropriate for capturing the cooling rates inherent to LPBF.

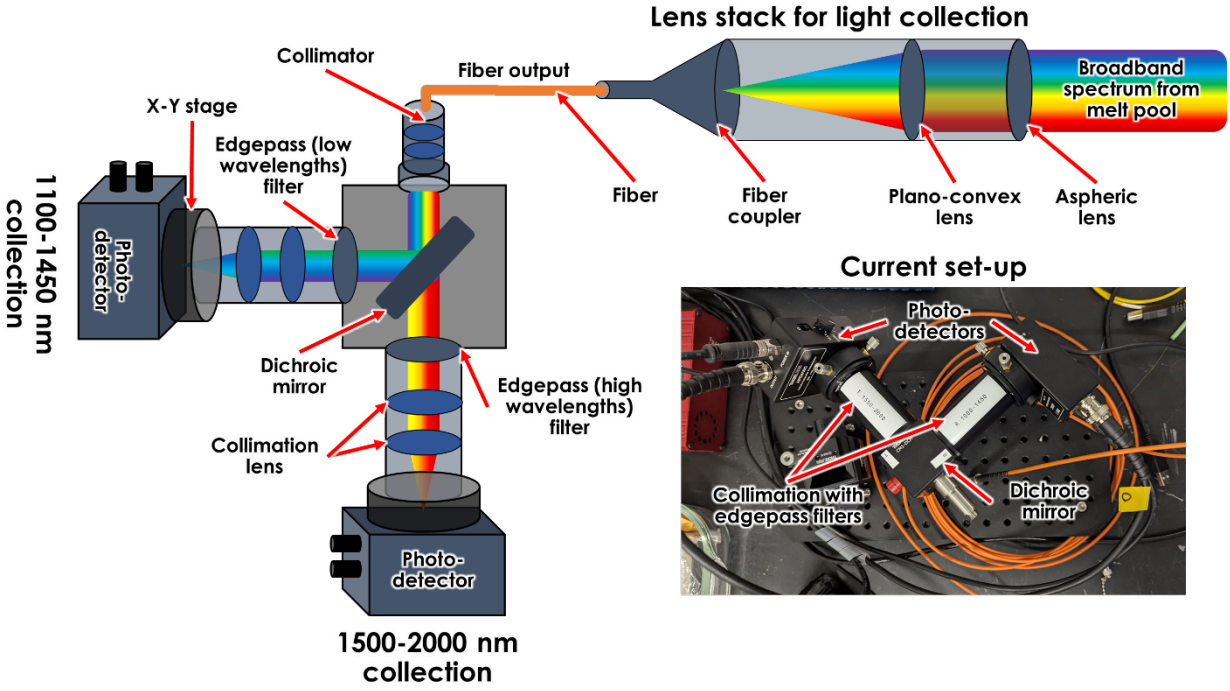

Figure 10. Schematic and photo of the optics and electronics of the pyrometer in the current configuration.

4.3 CALIBRATION IN OPTICAL DILATOMETER

Calibration of the pyrometer setup requires collection of a radiating spectrum for the desired material at a known temperature. It is difficult to find a furnace setup capable of going to a high temperature >1,200°C that is fitted with a sight glass for the pyrometer to view the sample. Therefore, the calibration was performed in an optical dilatometer as shown in Figure 11(a), designed to optically measure the thermal expansion of material to 1,700°C. The sight glass on the optical dilatometer is distanced from the sample by ~300 mm, as shown in Figure 11(a), in the furnace, and is adequately water cooled.

Viewing a molten SS316 composition was ideal, but the furnace is set up horizontally, making it difficult to contain molten metal. An SS316 sample was prepared by adhering an optically transparent sapphire tube (1.6 mm in diameter, 5.2 mm tall) to an alumina disk, as shown in Figure 11(b). The molten SS316 could then be contained in the tube and monitored with the pyrometer in the furnace as shown at Figure 11(c, d). The ratio of the low/high wavelength intensities collected during the calibration experiment are shown in Figure 11(e) and are compared to the model calculated from Eqs. (4)–(8), which include the responsivities of the APD detectors used. The data shown for the pyrometer in Figure 11(e) was taken with the notch filter included in the setup. Although the curves do not align on top of each other, the ratios are somewhat similar. It is expected that the addition of the edgepass filter will help improve the temperature ratio during calibration.

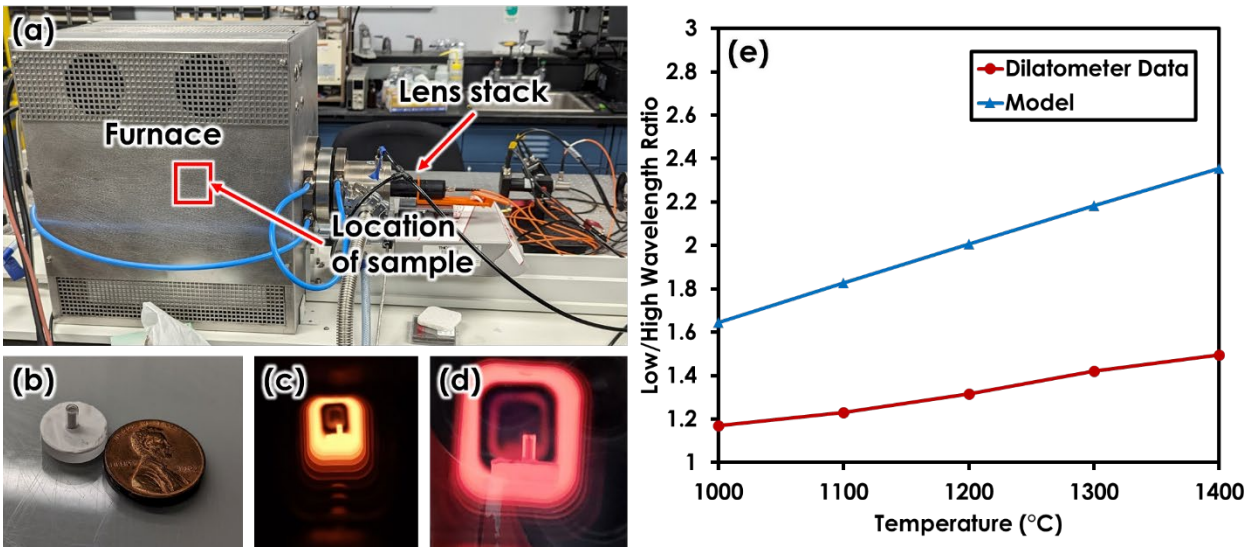

Figure 11. Calibrating the pyrometer to a temperature using an optical dilatometer. The pyrometer was (a) fitted to the sight glass within plain view of a sample. The sample used for calibration consisted of (b) a sapphire tube to house the molten SS316, adhered to an alumina disk (c, d); the sapphire tube at (c) 1,200°C and (d) 1,500°C; and (e) the low/high wavelength ratio collected during heating of the sapphire tube in the optical dilatometer as compared to the expected ratio calculated from the model.

4.4 IN-SITU MEASUREMENTS

For in-situ sensing inside the AM400 build chamber, the pyrometer is currently mounted in a plastic vise on the powder dispensing system, which is holding it ~150 mm from the top of the build plate as shown in Figure 12. The transmitted data are collected and sent via a fiber optic cable that is routed out of the build chamber using a feedthrough, as shown in Figure 12(a). The current field of view (effective spot size) of the pyrometer is 5 mm using the current free optics shown in Figure 10 and is highlighted in Figure 12(b).

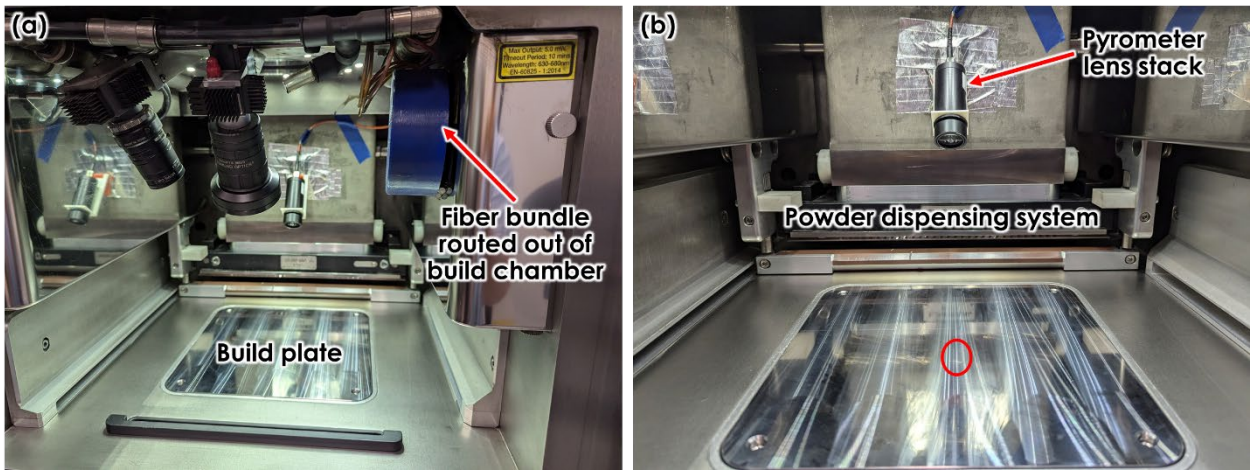

Figure 12. Configuration of the sensors in the AM400 build chamber showing the (a) the fiber bundle routed into the chamber, and (b) the placement of the pyrometer's lens stack for capturing light from the laser melting.

In-situ testing in the AM400 was performed on block geometries measuring 10 × 20 mm to ensure that the pyrometer fully collected the radiation from the printed material. This particular sample was printed with a dwell time of 30 µs. An example of in-situ data is shown in Figure 13 for a single layer of laser

melting of SS316 powder (layer thickness was 50 µm). The plots in Figure 13 focus on (a) 10,000 µs, (b) 1,000 µs, and (c) 60 µs of data. Figure 13(a) shows the vast amount data collected from a single printed layer, observing periodicity of the laser in Figure 13(b). By focusing closely on one single laser pulse, it can be observed that there is a large peak at the beginning of melting. Even with the notch filter installed, the low wavelength detector still seems to be measuring artifacts from the laser, as shown in Figure 13. It is likely that the initial peak represents a power dump by the laser during initial startup that lasted only ~200 ns. After this initial peak, the constant laser power can be observed for the 30 µs dwell time following by a 10 µs dead time in which the intensity decreases noticeably. Although the signal intensity from the melt pool is low compared to the laser signal, the gain can be increased on the photodetectors once the laser signal is cut out completely by an edgepass filter.

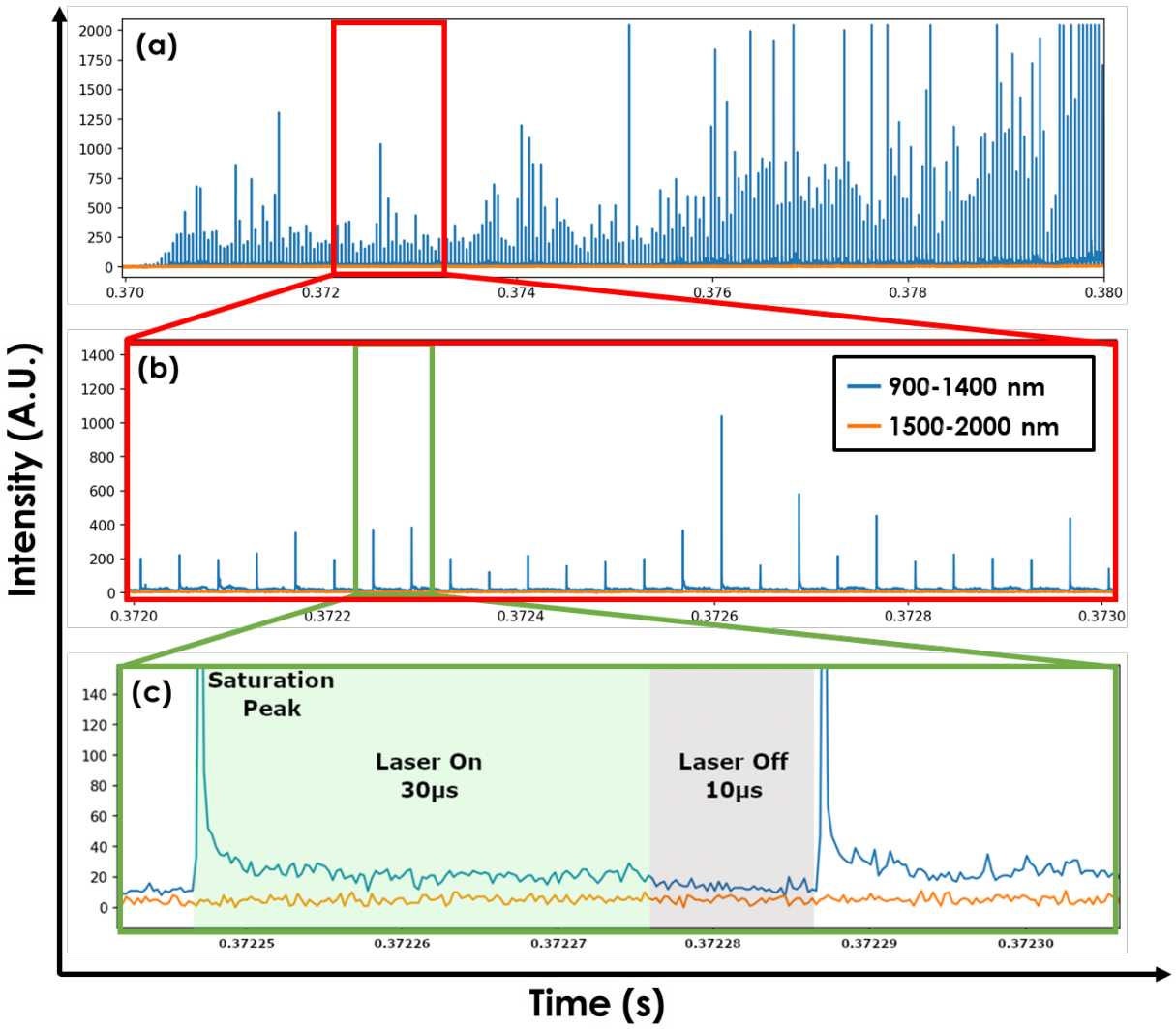

Figure 13. In-situ collection during laser melting in the Renishaw AM400 using the pyrometer setup before applying an edgepass filter to the low wavelength (900–1,400 nm) collection. (a) Collection of laser pulses over a 10,000 µs melting of one layer of SS316; (b) examination of the periodicity of the laser pulses over 1,000 µs observing an initial large intensity when the laser turns on; and (c) representative heating and cooling curves when the laser dwell time is on over the period of 30 µs.

5. MEASURING RESIDUAL STRESS

5.1 MOTIVATION FOR EX-SITU CHARACTERIZATION

Residual stress is a concern in LPBF because of the high cooling rates observed as illustrated in Figure 3. Two versions of SS316 are being investigated under the AMMT program [51]—SS316L and SS316H—the only difference being the carbon (C) content, which is 0.015 wt% C in SS316L and 0.08 wt% C in SS316H. Four 100 mm tall (and wide) plates were printed with a thickness of 15 mm on a 125 mm wide square build plate made of mild steel. The SS316L plates were printed with no issues. During printing of the same types of plates using SS316H at the same processing parameters, the wiper blade started interacting significantly with the build, and laser melting was observed to be much more extreme, so the build was stopped. The resulting build is shown in Figure 14(a). It was found that the build plate warped significantly, as shown in Figure 14(b), eventually popping the cap screws used to hold the build plate down on each corner, as shown in Figure 14(c).

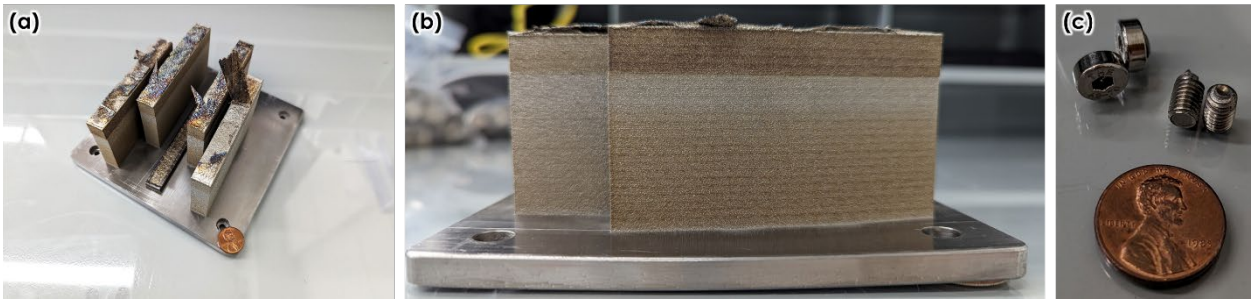

Figure 14. (a) An incomplete build containing four 100 mm tall plates printed from SS316H that failed because of overwhelming residual stress, causing (b) the plate to warp, and (c) the caps on the mounting screws to break off within the build volume.

Measuring residual stress in-situ is difficult, particularly when using unique setups with source-based systems such as those utilizing X-rays or neutrons. Resolving the evolved residual stress on components as large as 100 mm is nearly impossible for these techniques in situ. Therefore, residual stress differences between SS316L and SS316H were investigated ex-situ using neutron diffraction. As shown in Figure 15, a plate geometry was chosen for the study. The plate geometry consists of eight discrete segments, each of which was processed with a different energy density, as shown in Figure 15(a). The energy densities chosen were based on a large-scale process optimization study [51]. Each segment was joined at an interface that was 5 mm thick at the top and bottom of the plate. One single plate was chosen for processing to demonstrate the effects of varying energy density across a single component instead of analyzing eight separate components.

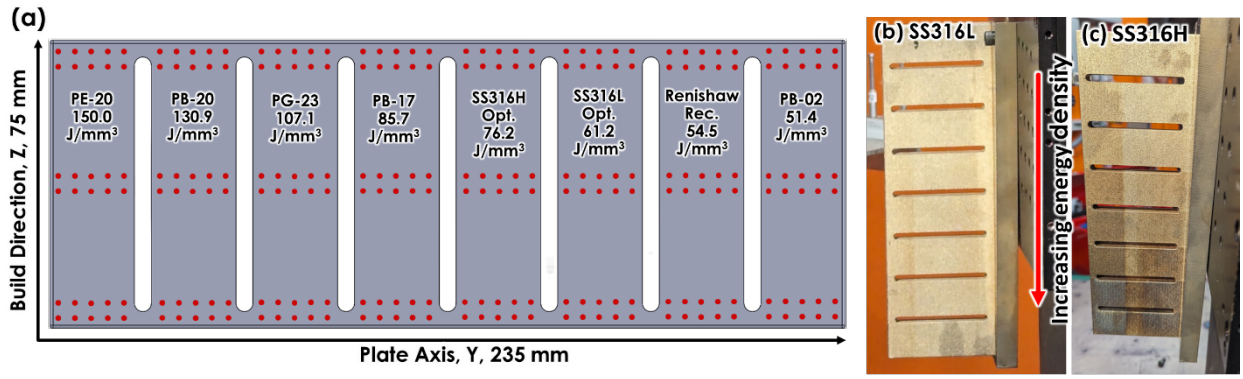

Figure 15. (a) Layout of plates printed from (b) SS316L and (c) SS316H, designed as eight discrete segments, each printed with a different energy density but joined together at the top and bottom to maintain one component.
Red points indicate the cuboid regions where the neutron beam was directed on each sample.

One of the builds was analyzed in Section 3.1. The plates were printed standing along the build direction, perpendicular to the build direction, and lying flat on the build plate. The plates processed from SS316L and SS316H are shown in Figure 15(b) and Figure 15(c), respectively. The samples standing along the build direction are the focus in this report. It has been observed that the plates have discoloration that is more intense with increasing energy density. Moreover, the SS316H exhibits darker gradients than the SS316L, even though the samples were processed with the same processing parameters.

5.2 HIDRA INSTRUMENT

The High Flux Isotope Reactor (HFIR) is an 85 MW research reactor with a peak thermal flux of 2.6×10^{15} neutrons/cm^2/s. Materials can be irradiated within the HFIR core to investigate the effects of radiation damage on experimental fuels or materials, or to produce isotopes. HFIR is also home to 12 beam line instruments for neutron diffraction. In fact, HFIR's current primary mission is related to neutron scattering. Among the 12 instruments is HIDRA, shown in Figure 16(a), which was specifically designed to measure residual stress in metals. HIDRA is set up with a quasi-2θ orientation aimed at 88–90° near the (311) and (222) peaks for face-centered cubic and body-centered cubic materials. The neutron flux of the beam line is 3.0×10^7 neutrons/cm^2/s, which is controlled using a double slit upstream of the beamline, as shown in Figure 16(b). For the purposes of this experiment, the plate samples were mounted with the 235 mm length aligned in the Z-direction with respect to the detector, as shown in Figure 16(c). Diffracted cuboids are indicated as red dots in Figure 15(a), which was a sum of 120 points per sample. A dwell time of 5 min was used for each point at a slit size of 2 × 4 mm.

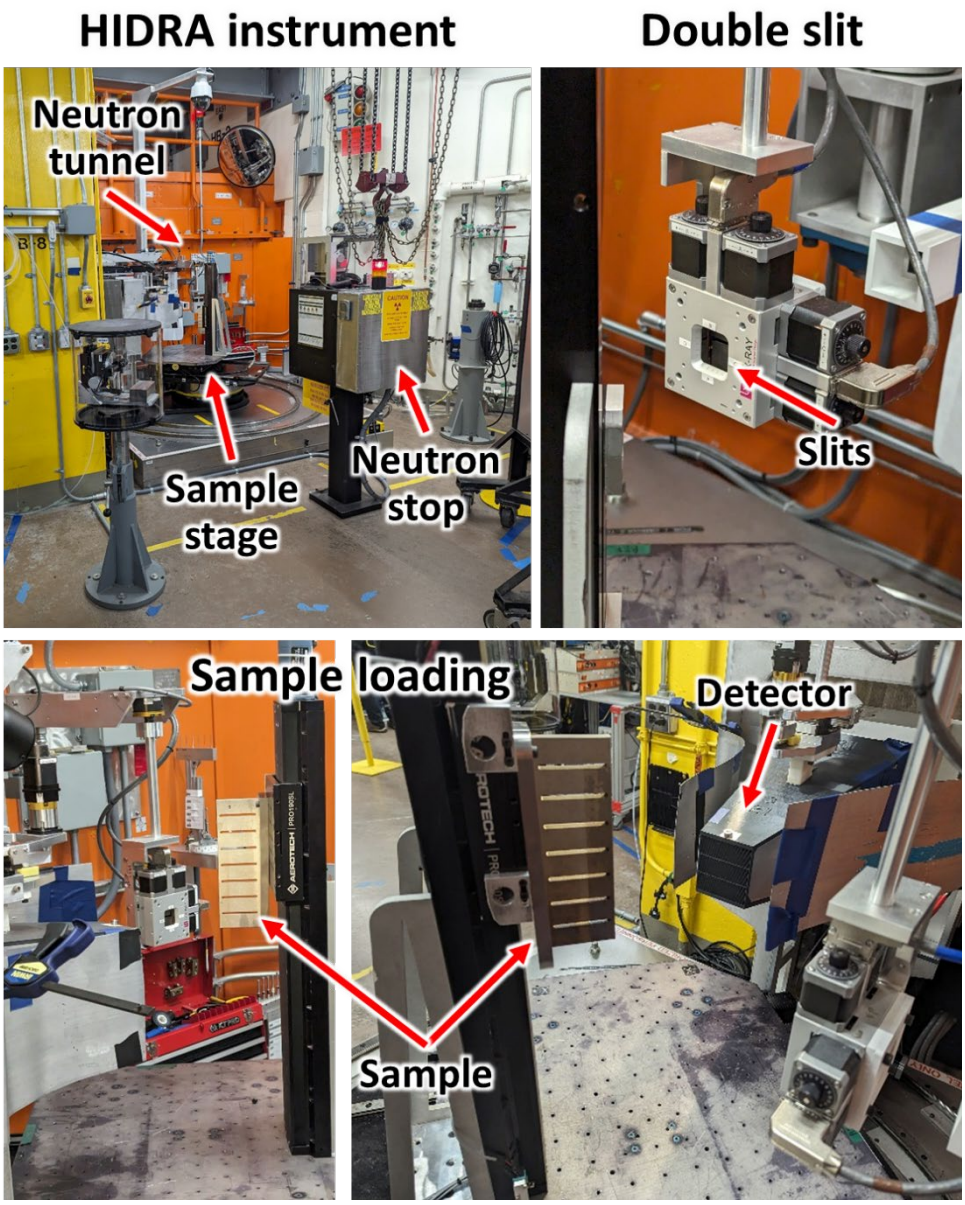

Figure 16. The HIDRA beamline instrument set up specifically for neutron diffraction of metals to measure residual stresses.

5.3 MAPPING STRESS AS A FUNCTION OF ENERGY DENSITY

The residual stresses collected from each cuboid on the SS316L and SS316H samples are mapped in Figure 17(a) and Figure 17(b), respectively. Because neutron diffraction could not be completed with the given time allotted for the experiment, the mappings in Figure 17 are represented as hex bins rather than creating an extrapolation to produce a heat map. More time is being set aside this summer to complete the neutron diffraction results for these specimens.

Overall, tensile stresses are observed at the edges of each segment, whereas compressive stresses are observed inside each segment. More compressive forces are observed at the top and center of each segment, and more tensile forces are seen near the bottom of the segments close to the build plate. The

laser's repeated local melting is expected to continuously induce a compressive stress. If the material is in compression, then the opposing forces must be towards the surface of the sample, similar to that observed in Figure 17.

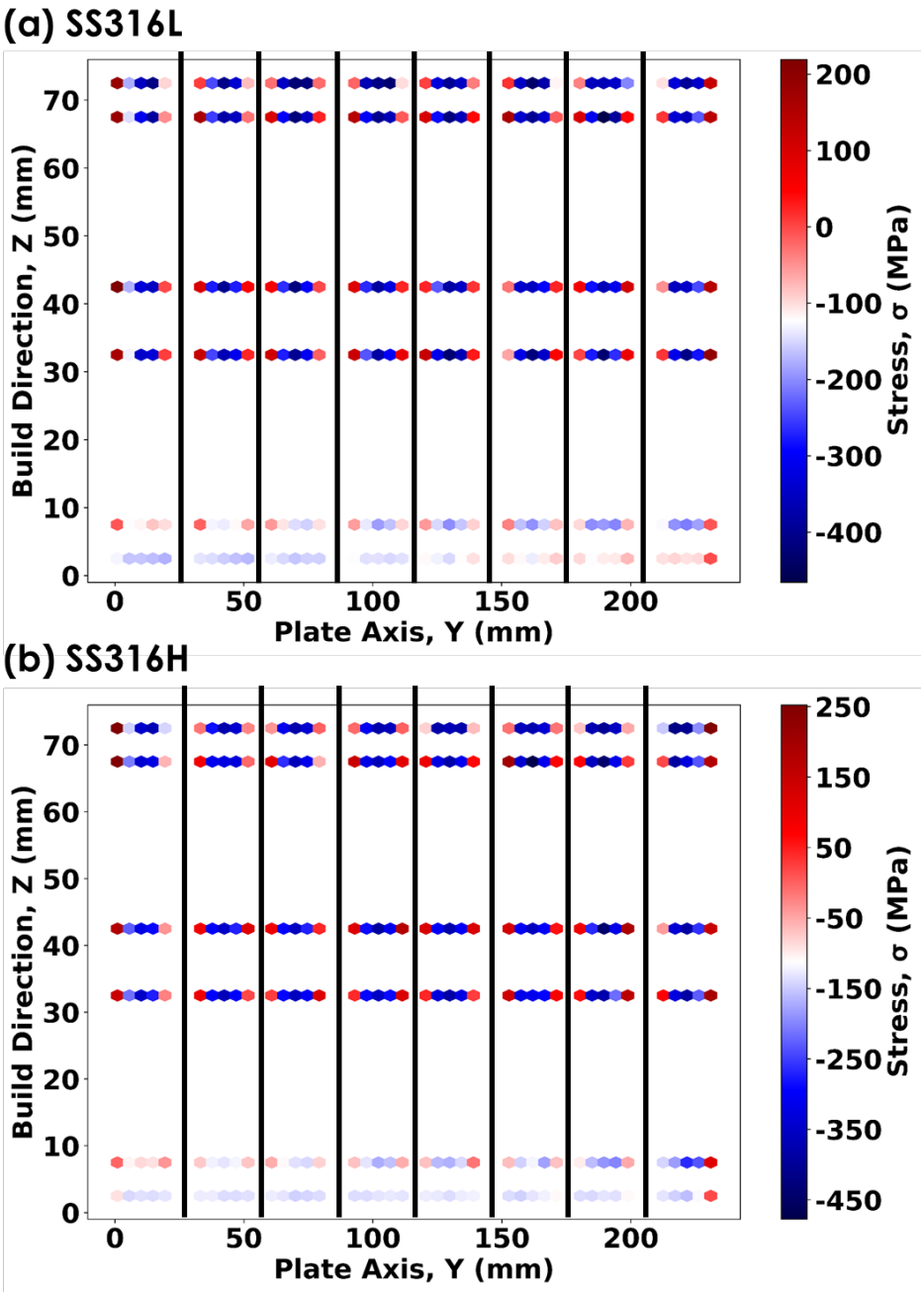

Figure 17. Mapped residual stress for (a) SS316L and (b) SS316H.

To further analyze the residual stress data, the average stress was taken for the middle points in each set of rows—top, center, and bottom—as shown in Figure 18(a). The middle point was expected to be most representative of the evolved stress within a printed component. Residual stress for the top, center, and bottom rows of points for both SS316L and SS316H is shown in Figure 18(b–d), respectively. Each segment is represented by the energy density used to print said segment. Generally, the stress appears to become more compressive with increasing energy density; this is expected because a high energy density,

higher heat input would be expected to induce higher compressive stresses. The stresses in the top and center points, shown in Figure 18(b) and Figure 18(c), respectively, have similar magnitudes of stress, but the bottom points were clearly more tensile in nature. Although minor, stress in SS316H appear to be more tensile in nature than those in SS316L. The additional neutron diffraction time will include longer scans to produce higher quality data that should help resolve the differences between SS316L and SS316H.

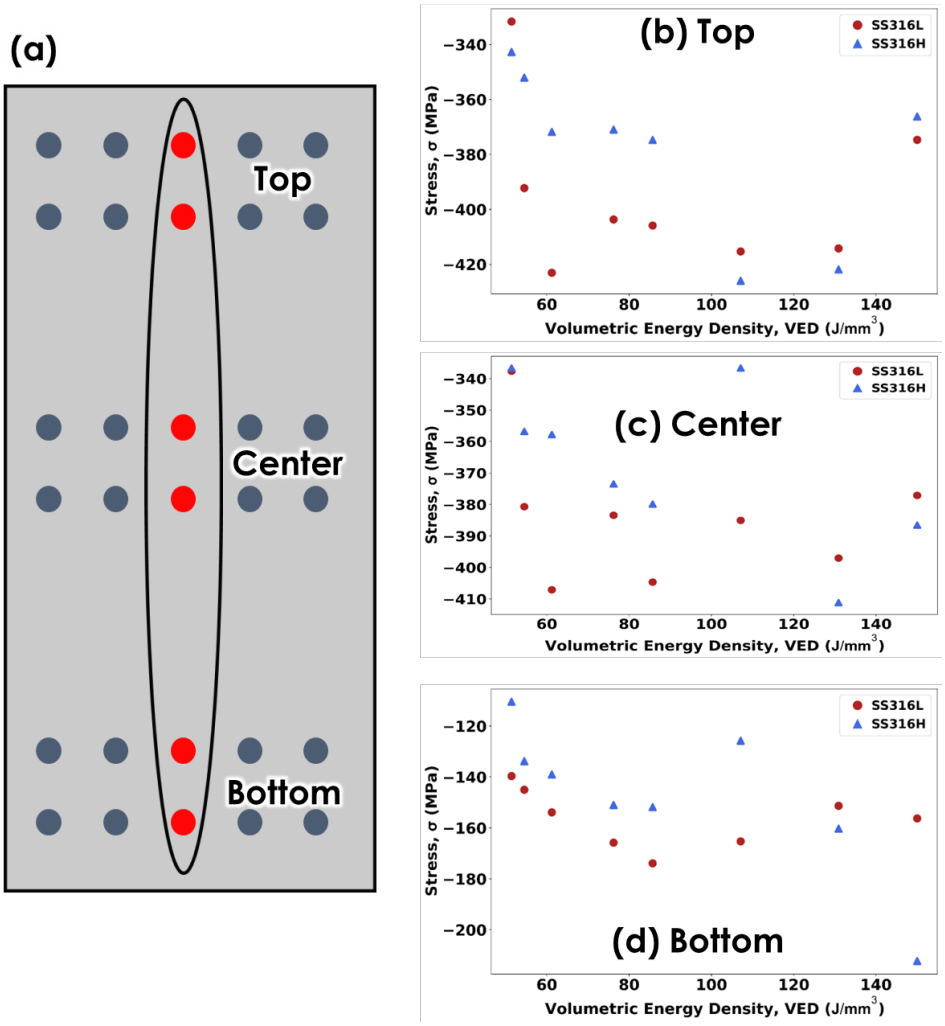

Figure 18. Residual stress as a function of energy density for the (a) middle data points taken in each section: (b–d) average stress plotted for SS316L vs. SS316H at the (b) top, (c) center, and (d) bottom rows of points.

5.4 MONITORING STRESS ACCUMULATION WITH ACOUSTIC SENSING

It is difficult to measure evolved stress during LPBF processing. It is known that high residual stresses could cause warpage, delamination, or cracking—all major defects in the LPBF process. Many of these defects may not be immediately detected by process anomaly monitoring because cracking or onsets of delamination are often internal to a component or not visible at the top of the build plane. Process anomaly classifications such as edge swelling or over melting may indicate some potential concerns for users to monitor, but currently these factors cannot be used to fully predict whether those anomalies will cause major defects or build failure.

Eddy-current and acoustic waveforms have been used for decades to detect cracking or large pores in welds or surfaces of pipes or vessels. Commercial LPBF machines are host to many vibrations, including vibrations from continuous gas flow across the powder bed. The system vibrations could be monitored using acoustic sensors such as accelerometers.

Accelerometers are widely used across numerous applications and are commercially available in varying shapes and sizes. Low-profile accelerometers can be mounted near a build plate or in the build volume with an organized distribution, as shown in Figure 19. Components that begin to exhibit cracking or other potential defects such as delamination would change the acoustic signature relative to a baseline signal that could be recorded at the start of a build. Defects would most likely lead to lower frequency peaks with higher amplitude, as shown in Figure 19. Ideally, the accelerometers could be used to triangulate defects in components, but that could prove challenging. At a minimum, these sensors could be easily integrated into commercial machines to detect the onset of failure or a major defect that a process anomaly detection software may not be able to visualize.

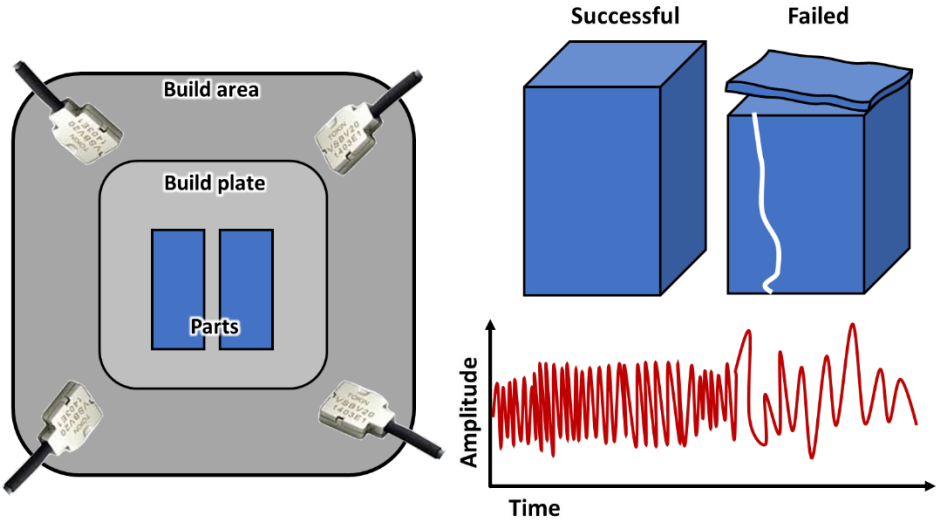

Figure 19. Using accelerometers distributed around a build plate to detect changes in the acoustic amplitude of the system that could be correlated to major defects such as cracking or delamination.

6. SUMMARY

The nuclear industry could greatly benefit from the geometric freedom offered by AM processes such as LPBF. However, the process of qualifying new materials for nuclear applications is complex and time-consuming, and it is made even more challenging without an established framework for AM processes, inherently resulting in significant heterogeneities in the materials. For example, LPBF cooling rates are expected to be higher by multiple orders of magnitude than those of conventional manufacturing techniques, yielding a high degree of heterogeneity in the microstructure, and subsequently, anisotropy in the materials performance (e.g., mechanical behavior). A paradigm collecting in-situ data, materials characterization, and advanced machine learning algorithms was developed under the TCR program; the legacy being the digital platform in which material and printed components can be tracked from feedstock to deployment in application. Current in-situ monitoring systems integrated into the digital platform include process anomaly detection by classifying voxels from images taken of the build before and after laser melting. However, the correlation between the detected anomalies and resulting microstructure and materials performance is still somewhat unknown. Therefore, investigation of other in-situ monitoring techniques is warranted to understand more fundamental information about the LPBF process including

the thermal history and stress state of the system. Ultimately techniques like those described here will be used as part of a broader process to understand and qualify AM components for nuclear applications.

The different in-situ monitoring systems investigated, and their current status is listed below:

1. Two cameras, visible and near IR, were outfitted on a Renishaw AM400 for the dual imaging technique already established at ORNL under the TCR program. The DMSCNN neural network used to detect process anomalies is currently still immature, but has already shown the ability to detect typical process anomalies such as powder spatter or edge swelling in large builds. To compliment the sensor suite on the AM400, a fringe imaging system is being outfitted on a Renishaw AM250, operating similar to the AM400, as method of producing a topographic profile of the powder bed during printing, and detect anomalies that way. A fringe system is being procured from the company Phase3D, who already has a presence in industry, outfitting various commercial LPBF machines.

2. A two-color pyrometer was developed to measure the melt pool temperatures experienced during laser melting, collecting at acquisitions rates (10^7 1/s) similar to that of the cooling rates inherent to LPBF (10^6–10^7 K/s). Iterations on the pyrometer included first using commercially available WDMs to split the collected spectrum into two discrete wavelengths to take a ratio between for calibration to a temperature, but ultimately not finding enough intensity at the single wavelengths. Eventually, free space optics were used to collect and collimate the broad-band spectrum emitted by the laser melting process; the collected spectrum being split into two separate wavelength ranges (900–1,450 nm and 1,500–2,000 nm) using a dichroic mirror, which improved signal greatly. Edgepass filters are used to ensure that any intensity from the laser wavelength (1,070 nm) does not obscure the signal, before being directed to a fine point on variable gain APD InGaAs photodetectors. Initial in-situ monitoring with the pyrometer inside the AM400 during laser melting showed that the on/off pulsing of the laser could be accurately monitored. Future work will be performed with the newest set-up of the pyrometer to collect higher quality data and start to calibrate to a temperature using a calibration curve taken with molten SS316 during heating in an optical dilatometer.

3. It has been established that the thermal history of the printed component will greatly influence the microstructure and mechanical performance, but it will also influence the stress state. Higher stresses may overcome the yield strength of the material, leading to defects such as cracking, or warpage, or delamination of layers. Ex-situ characterization data was collected on SS316L and SS316H using neutron diffraction to show influential minor compositional changes and varying energy densities can influence the stress state of LPBF material. Overall, it was observed that high energy densities, i.e., higher heat inputs, resulted in more compressive stresses, whereas lower energy densities, i.e., lower heat inputs, result in more tensile stresses. Measuring the evolved stress-state in-situ is difficult and would most likely require using a source like neutrons, not easily done or cost-effective for every build performed. Waveform detection methods such as acoustic or eddy-current have shown to detect defects like cracks in welds across multiple industries. Rather than measuring the evolved stress of the system, simple accelerometer-based sensors can be installed in or around the powder volume to monitor acoustic profile of the system (i.e., vibrations) to look for changes in modes. Under continuous operation, functions like the gas recirculation pump will induce enough vibrations to give the system a constant background profile, most likely full of high intensity, low amplitude peaks. Cracking, warpage, or delamination would ultimately change the modes in the system, causing lower frequency peaks with large amplitudes. These rapid detection methods can be implemented to immediately alert the operator to a fatal defect that may not be observed by the process anomaly detection system.

7. REFERENCES

[1] G.S. Was, D. Petti, S. Ukai, S. Zinkle, Materials for future nuclear energy systems, Journal of Nuclear Materials 527 (2019) 151837.
[2] S.J. Zinkle, K.A. Terrani, L.L. Snead, Motivation for utilizing new high-performance advanced materials in nuclear energy systems, Current Opinion in Solid State and Materials Science 20(6) (2016) 401-410.
[3] S.J. Zinkle, G.S. Was, Materials challenges in nuclear energy, Acta Materialia 61(3) (2013) 735-758.
[4] R.N. Wright, Updated draft ASME boiler and pressure vessel code case for use of Alloy 617 for construction of nuclear components for section III division 5, Idaho National Lab.(INL), Idaho Falls, ID (United States), 2018.
[5] T.-L. Sham, R.E. Bass, Y. Wang, X. Zhang, A709 Qualification Plan Update and Mechanical Properties Data Assessment, Idaho National Lab.(INL), Idaho Falls, ID (United States), 2022.
[6] T.-L. Sham, K. Natesan, Code qualification plan for an advanced austenitic stainless steel, alloy 709, for sodium fast reactor structural applications, (2017).
[7] S. Cetiner, P. Ramuhalli, Transformational Challenge Reactor Autonomous Control System Framework and Key Enabling Technologies, United States, 2019, p. Medium: ED.
[8] B. Betzler, B. Ade, A. Wysocki, P. Jain, P. Chesser, M. Greenwood, K. Terrani, Transformational Challenge Reactor preconceptual core design studies, Nuclear Engineering and Design 367 (2020) 110781.
[9] B.R. Betzler, B.J. Ade, P.K. Jain, A.J. Wysocki, P.C. Chesser, W.M. Kirkland, M.S. Cetiner, A. Bergeron, F. Heidet, K.A. Terrani, Conceptual Design of the Transformational Challenge Reactor, Nuclear Science and Engineering (2022) 1-26.
[10] N. See, S. Cetiner, B. Betzler, Design Optimization of the Transformational Challenge Reactor Outlet Plenum, Nuclear Science and Engineering (2022) 1-20.
[11] B. Ade, B. Betzler, A. Wysocki, J. Weinmeister, N. See, P. Jain, W. Kirkland, J. Burns, B. Hiscox, D. Schappel, A. Talamo, A. Bergeron, C.J. Jessee, Transformational Challenge Reactor Design Characteristics, Conference: PHYSOR 2022: International Conference on Physics of Reactors 2022 - Oak Ridge, Tennessee, United States of America - 5/15/2022 8:00:00 AM-5/20/2022 8:00:00 AM, United States, 2022, p. Medium: ED.
[12] B.R. Betzler, B.J. Ade, A. Wysocki, P. Chesser, M.S. Greenwood, P. Wang, N. See, X. Hu, K. Terrani, Design Downselection for the Transformational Challenge Reactor, Oak Ridge National Lab. (ORNL), Oak Ridge, TN (United States), 2020.
[13] B.R. Betzler, B.J. Ade, A.J. Wysocki, P.K. Jain, P.C. Chesser, M.S. Greenwood, K.A. Terrani, Transformational Challenge Reactor preconceptual core design studies, Nucl. Eng. Des. 367 (2020) 110781.
[14] M. Messner, B. Barua, A. Huning, S. Arndt, C. Massey, S. Taller, R. Dehoff, M. Russell, L. Scime, Z. Snow, ASME Code Qualification Plan for LPBF 316 SS, Argonne National Laboratory (ANL), Argonne, IL (United States), 2023.
[15] M. Li, D. Andersson, R. Dehoff, A. Jokisaari, I. van Rooyen, D. Cairns-Gallimore, Advanced Materials and Manufacturing Technologies (AMMT) 2022 Roadmap, Argonne National Lab.(ANL), Argonne, IL (United States), 2022.
[16] W.J. Sames, F. List, S. Pannala, R.R. Dehoff, S.S. Babu, The metallurgy and processing science of metal additive manufacturing, International Materials Reviews 61(5) (2016) 315-360.
[17] H. Hyer, L. Zhou, A. Mehta, S. Park, T. Huynh, S.T. Song, Y.L. Bai, K. Cho, B. McWilliams, Y. Sohn, Composition-dependent solidification cracking of aluminum-silicon alloys during laser powder bed fusion, Acta Materialia 208 (2021) 116698.
[18] H. Hyer, L. Zhou, S. Park, G. Gottsfritz, G. Benson, B. Tolentino, B. McWilliams, K. Cho, Y. Sohn, Understanding the Laser Powder Bed Fusion of AlSi10Mg Alloy, Metallography Microstructure and Analysis 9(4) (2020) 484-502.

[19] H.C. Hyer, C.M. Petrie, Effect of powder layer thickness on the microstructural development of additively manufactured SS316, Journal of Manufacturing Processes 76 (2022) 666-674.
[20] L. Scime, C. Joslin, D.A. Collins, M. Sprayberry, A. Singh, W. Halsey, R. Duncan, Z. Snow, R. Dehoff, V. Paquit, A Data-Driven Framework for Direct Local Tensile Property Prediction of Laser Powder Bed Fusion Parts, Materials 16(23) (2023) 7293.
[21] L. Scime, M. Sprayberry, D. Collins, A. Singh, C. Joslin, R. Duncan, J. Simpson, F. List III, K. Carver, A. Huning, Diagnostic and Predictive Capabilities of the TCR Digital Platform, (2021).
[22] Y. AbouelNour, N. Gupta, In-situ monitoring of sub-surface and internal defects in additive manufacturing: A review, Materials & Design (2022) 111063.
[23] H.-H. König, N.H. Pettersson, A. Durga, S. Van Petegem, D. Grolimund, A.C. Chuang, Q. Guo, L. Chen, C. Oikonomou, F. Zhang, G. Lindwall, Solidification modes during additive manufacturing of steel revealed by high-speed X-ray diffraction, Acta Materialia 246 (2023) 118713.
[24] A. Ziabari, S.V. Venkatakrishnan, Z. Snow, A. Lisovich, M. Sprayberry, P. Brackman, C. Frederick, P. Bhattad, S. Graham, P. Bingham, R. Dehoff, A. Plotkowski, V. Paquit, Enabling rapid X-ray CT characterisation for additive manufacturing using CAD models and deep learning-based reconstruction, npj Computational Materials 9(1) (2023) 91.
[25] L. Scime, J. Beuth, Anomaly detection and classification in a laser powder bed additive manufacturing process using a trained computer vision algorithm, Additive Manufacturing 19 (2018) 114-126.
[26] L. Scime, B. Fisher, J. Beuth, Using coordinate transforms to improve the utility of a fixed field of view high speed camera for additive manufacturing applications, Manufacturing Letters 15 (2018) 104-106.
[27] L. Scime, D. Siddel, S. Baird, V. Paquit, Layer-wise anomaly detection and classification for powder bed additive manufacturing processes: A machine-agnostic algorithm for real-time pixel-wise semantic segmentation, Additive Manufacturing 36 (2020) 101453.
[28] L. Scime, A. Singh, V. Paquit, A scalable digital platform for the use of digital twins in additive manufacturing, Manufacturing Letters 31 (2022) 28-32.
[29] Z. Snow, L. Scime, A. Ziabari, B. Fisher, V. Paquit, Observation of spatter-induced stochastic lack-of-fusion in laser powder bed fusion using in situ process monitoring, Additive Manufacturing 61 (2023) 103298.
[30] Y. Kok, X.P. Tan, P. Wang, M. Nai, N.H. Loh, E. Liu, S.B. Tor, Anisotropy and heterogeneity of microstructure and mechanical properties in metal additive manufacturing: A critical review, Materials & Design 139 (2018) 565-586.
[31] Z. Gan, O.L. Kafka, N. Parab, C. Zhao, L. Fang, O. Heinonen, T. Sun, W.K. Liu, Universal scaling laws of keyhole stability and porosity in 3D printing of metals, Nature Communications 12(1) (2021) 2379.
[32] Y. Huang, T.G. Fleming, S.J. Clark, S. Marussi, K. Fezzaa, J. Thiyagalingam, C.L.A. Leung, P.D. Lee, Keyhole fluctuation and pore formation mechanisms during laser powder bed fusion additive manufacturing, Nature Communications 13(1) (2022) 1170.
[33] H. Hyer, L. Zhou, S. Park, G. Gottsfritz, G. Benson, B. Tolentino, B. McWilliams, K. Cho, Y. Sohn, Understanding the Laser Powder Bed Fusion of AlSi10Mg Alloy, Metallography, Microstructure, and Analysis 9 (2020) 484-502.
[34] S.S. Babu, N. Raghavan, J. Raplee, S.J. Foster, C. Frederick, M. Haines, R. Dinwiddie, M.K. Kirka, A. Plotkowski, Y. Lee, R.R. Dehoff, Additive Manufacturing of Nickel Superalloys: Opportunities for Innovation and Challenges Related to Qualification, Metallurgical and Materials Transactions A 49(9) (2018) 3764-3780.
[35] J. Raplee, A. Plotkowski, M.M. Kirka, R. Dinwiddie, A. Okello, R.R. Dehoff, S.S. Babu, Thermographic Microstructure Monitoring in Electron Beam Additive Manufacturing, Scientific Reports 7(1) (2017) 43554.

[36] H. Hyer, L. Zhou, A. Mehta, S. Park, T. Huynh, S. Song, Y. Bai, K. Cho, B. McWilliams, Y. Sohn, Composition-Dependent Solidification Cracking of Aluminum-Silicon Alloys During Laser Powder Bed Fusion, Acta Materialia 208 (2021) 116698.
[37] L. Zhou, H. Hyer, S. Thapliyal, R.S. Mishra, B. McWilliams, K. Cho, Y. Sohn, Process-Dependent Composition, Microstructure, and Printability of Al-Zn-Mg and Al-Zn-Mg-Sc-Zr Alloys Manufactured by Laser Powder Bed Fusion, Metallurgical and Materials Transactions A 51(6) (2020) 3215-3227.
[38] C.M. Petrie, N. Sridharan, In situ measurement of phase transformations and residual stress evolution during welding using spatially distributed fiber-optic strain sensors, Measurement Science and Technology 31(12) (2020) 125602.
[39] M. Seleznev, T. Gustmann, J.M. Friebel, U.A. Peuker, U. Kühn, J.K. Hufenbach, H. Biermann, A. Weidner, In situ detection of cracks during laser powder bed fusion using acoustic emission monitoring, Additive Manufacturing Letters 3 (2022) 100099.
[40] J.R. Tempelman, A.J. Wachtor, E.B. Flynn, P.J. Depond, J.-B. Forien, G.M. Guss, N.P. Calta, M.J. Matthews, Sensor fusion of pyrometry and acoustic measurements for localized keyhole pore identification in laser powder bed fusion, Journal of Materials Processing Technology 308 (2022) 117656.
[41] K. Gutknecht, M. Cloots, R. Sommerhuber, K. Wegener, Mutual comparison of acoustic, pyrometric and thermographic laser powder bed fusion monitoring, Materials & Design 210 (2021) 110036.
[42] M. Rolchigo, J. Coleman, G.L. Knapp, A. Plotkowski, Grain structure and texture selection regimes in metal powder bed fusion, Additive Manufacturing 81 (2024) 104024.
[43] M.C. Flemings, Solidification processing, McGraw-Hill1974.
[44] S. Kou, Welding metallurgy, 2nd Edition ed., John Wiley & Sons2003.
[45] W. Halsey, D. Rose, L. Scime, R. Dehoff, V. Paquit, Localized defect detection from spatially mapped, in-situ process data with machine learning, Frontiers in Mechanical Engineering 7 (2021) 767444.
[46] A. Huning, R. Fair, A. Coates, V. Paquit, L. Scime, M. Russell, K. Kane, S. Bell, B. Lin, B. Betzler, Digital Platform Informed Certification of Components Derived from Advanced Manufacturing Technologies, Oak Ridge National Lab.(ORNL), Oak Ridge, TN (United States), 2021.
[47] L. Scime, J. Haley, W. Halsey, A. Singh, M. Sprayberry, A. Ziabari, V. Paquit, Development of Monitoring Techniques for Binderjet Additive Manufacturing of Silicon Carbide Structures, United States, 2020, p. Medium: ED; Size: 44 p.
[48] L. Scime, J. Haley, W. Halsey, A. Singh, M. Sprayberry, A. Ziabari, V. Paquit, Report on Progress of correlation of in-situ and ex-situ data and the use of artificial intelligence to predict defects, United States, 2020, p. Medium: ED; Size: 53 p.
[49] A. Tapetado, J. Diaz-Alvarez, H. Miguelez, C. Vázquez, Fiber-optic pyrometer for very localized temperature measurements in a turning process, IEEE Journal of selected topics in Quantum Electronics 23(2) (2016) 278-283.
[50] B. Müller, U. Renz, Development of a fast fiber-optic two-color pyrometer for the temperature measurement of surfaces with varying emissivities, Review of scientific instruments 72(8) (2001) 3366-3374.
[51] C. Massey, P. Nandwana, H. Hyer, S. Nayir, J. Kendall, C. Joslin, R. Duncan, D. Collins, T. Graening Seibert, F. List III, L. Scime, Z. Snow, A. Ziabari, T. Butcher, R. Dehoff, Data-Driven Optimization of the Processing Window for 316H Components Fabricated Using Laser Powder Bed Fusion, Oak Ridge National Laboratory, ak Ridge National Laboratory, 2023.